energies

MDPI

Article

Model-Predictive Energy Management for Optimizing the System Efficiency of a Fuel Cell Truck Considering Fuel Cell Degradation

Simon Mertes [1,2,*], Alexander Wehren [1,2], Vivek Srivastava [3], Joschka Schaub [3], Alexandre Ennen [1,2] and Stefan Pischinger [1,2]

[1] Chair of Thermodynamics of Mobile Energy Conversion Systems (TME), RWTH Aachen University, Forckenbeckstraße 4, 52074 Aachen, Germany; wehren@tme.rwth-aachen.de (A.W.); ennen@tme.rwth-aachen.de (A.E.)
[2] Center for Mobile Propulsion (CMP), RWTH Aachen University, Forckenbeckstraße 4, 52074 Aachen, Germany
[3] FEV Europe GmbH, Neuenhofstraße 181, 52078 Aachen, Germany; srivastava@fev.com (V.S.); schaub@fev.com (J.S.)
* Correspondence: mertes_s@tme.rwth-aachen.de; Tel.: +49-241-80-24207

Abstract

This work presents a model predictive control (MPC) approach for optimizing the powertrain system efficiency of a fuel cell electric heavy-duty vehicle. The MPC determines the power split between the high-voltage traction battery and the fuel cell system so that the power demand of the drive cycle is met, while a second objective extends the lifetime of the fuel cell stack by including stack degradation in the cost function. Based on driving profile information, the controller adjusts the fuel cell power trajectory within a specified prediction horizon such that a target state of charge of the traction battery is reached at the end of the time-discrete horizon, fuel consumption is minimized, and excessive degradation is avoided. The control variables are computed from discrete-time models of the fuel cell, the truck, and the battery. The resulting non-linear optimization problem is solved with the open-source software package `acados`, integrated into `MATLAB Simulink` to achieve real-time capability. The MPC is implemented and tested in a model-in-the-loop environment, and its real-time execution is verified on a dSPACE MicroAutoBox III rapid control prototyping unit. On the Vehicle Energy Consumption Calculation Tool (VECTO) Long Haul cycle, hydrogen consumption is reduced by 6.5%, while membrane thinning and the loss of electrochemically active surface area are reduced by 6.1% and 2.3%, respectively, compared with a rule-based strategy.

Keywords: energy management strategy; model predictive control; fuel cell system; degradation; heavy-duty vehicle; hydrogen consumption; state of health; nonlinear optimization; real-time capability; state of charge

Check for updates

Academic Editors: Felix Barreras and JongHoon Kim

Received: 12 August 2026
Revised: 29 September 2026
Accepted: 19 October 2026
Published: 22 October 2026

Copyright: © 2026 by the authors. Licensee MDPI, Basel, Switzerland. This article is an open access article distributed under the terms and conditions of the Creative Commons Attribution (CC BY) license.

1. Introduction and Motivation

In order to comply with the maximum global temperature increase of 2 K by 2050 set by the Paris Climate Agreement in 2015, the European Union (EU) has formulated greenhouse gas emission limits for the transportation sector [1]. According to 2016 data, heavy-duty commercial vehicles are responsible for 27% of CO_2 emissions from road transport and around 5% of greenhouse gas emissions in the EU, according to a press release from the European Parliament [2]. This is due to the increase in freight transport since 1990, which has

increased CO_2 emissions from heavy-duty vehicles by 25%. Electric powertrain architectures offer a future-proof solution for meeting greenhouse gas emissions regulations in all possible transport sectors [3]. The transition from fossil fuels to environmentally friendly energy sources introduces new challenges that must be addressed to meet consumer and regulatory demands.

In addition to electrified powertrains, so-called electric vehicles (EVs), fuel cell electric vehicles (FCEVs) in particular offer a promising solution in terms of zero local CO_2 emissions, higher energy density, and faster recharging compared to battery electric vehicles [3,4]. The reduction of greenhouse gas emissions can be achieved through the integration of a fuel cell and green hydrogen [5] within a powertrain application. In an all-electric FCEV, the fuel cell is the primary energy source [6]. With more than one energy source, an FCEV uses a combination of a fuel cell system and an energy storage system (ESS), preferably a high-voltage (HV) traction battery or supercapacitors (SC), to compensate for the slow dynamics of the fuel cell during load changes and to enable the regenerative recovery of braking energy [6,7]. It is evident that fuel cell systems represent a viable option for achieving CO_2-neutral mobility, particularly in the context of heavy-duty vehicles [8]. In order to operate a hybrid system with multiple energy sources in an efficient way, an active energy management strategy (EMS) is required. In the case of fuel cell operation, the power distribution must be optimized to operate at the most efficient point, taking into account system constraints and durability [3,4].

1.1. Energy Management Strategies

EMSs are operating strategies that attempt to efficiently meet various powertrain requirements, taking into account the optimal use of multiple energy sources. EMSs are used to improve the performance of hybrid vehicles in terms of both energy consumption and component lifetime [7].

EMSs can be classified into three groups: rule-based, optimization-based, and learning-based EMSs. The proposed methods have their own advantages and limitations, which are discussed individually in the following section. Figure 1 provides an overview of the most frequently used optimization algorithms, classified according to their real-time capability and their potential for optimization over the prediction horizon.

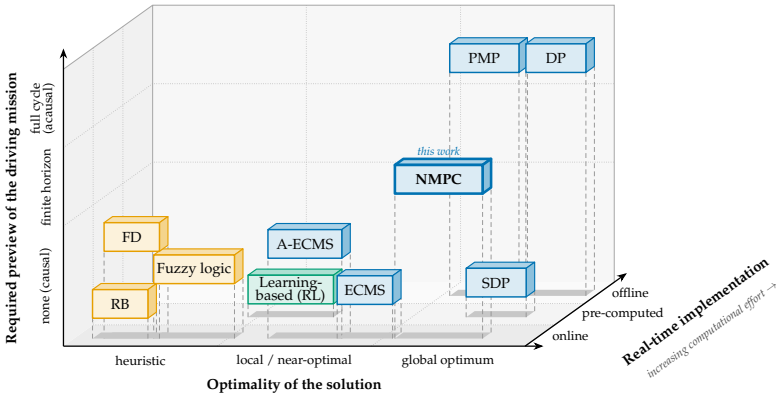


Figure 1. General comparison of studied EMSs [4].

To reduce the load change rate of the fuel cell system [9], a series of fuzzy control strategies were used. As a result, the load change rate is reduced and limited to the range of change capacity. Fuzzy-logic (FL) control is an extension of conventional rule-based (RB) control based on if-else conditions that attempt to recreate the human decision-making process [10]. Another type of RB-EMS is frequency decoupling, which splits the power demand in the frequency domain so that the high-frequency demand is met by the battery and

the low-frequency demand is met by the fuel cell [9,11]. A recent example is given in [12] for a fuel cell/battery/ultracapacitor system, in which the fuel cell power reference is derived from a proportional-integral (PI) controller acting on the state of charge (SoC) deviation and the transient share is separated by frequency decoupling. The adaptation in this approach acts on the gains of the converter controllers (adaptive and fractional-order PI control, internal model control) and is evaluated in terms of direct current (DC) bus voltage regulation, overshoot, and settling time on a laboratory-scale system, i.e., at the power electronics control level rather than at the level of drive cycle hydrogen consumption. This method has been extended by [13] with an optimization-based strategy to consider not only the dynamic requirements but also the energy efficiency in terms of fuel consumption and SoC management.

Rule-based strategies can be implemented with little effort, since they require neither a plant model nor training data, and their rules can operate on both directly measured and model-based signals. They have a low computation time due to the stationary control decisions based on the input values. However, the heuristic strategies require a high calibration effort in order to guarantee a performance close to optimality for each driving cycle. In addition, the rules are not easily scalable to different powertrain architectures or different component sizes [14].

Learning-based (LB) EMS uses data mining methods that utilize historical and real-time information from large amounts of data to derive the optimal control law.

An intelligent energy management concept that employs training data to determine the best power control for a hybrid vehicle system with three or more energy sources and significant load fluctuations is presented in [15]. The machine learning algorithm covers a wide range of power requirements with restrictions in terms of system voltage and keeping the states of charge of the energy storage units within predefined thresholds. By optimally combining the energy sources, the power losses of the overall system were reduced by 28% up to 76% compared to a conventional rule-based power control [15].

Reinforcement learning (RL) is presented in [16], taking into account the lifetime of the fuel cell system. The RL algorithm is pre-initialized by energy allocation rules to speed up the optimization process. Simulation results show that the average H_2 consumption difference between the proposed EMS and an EMS based on dynamic programming (DP) is 5.59% in the training and validation driving cycles. In addition, the proposed EMS reduces the average power difference of the fuel cell system, which should also reduce the performance degradation. Compared to a conventional RL-based EMS, which does not take into account the lifetime of the fuel cell system, the power fluctuations could be reduced by at least 13%. This is a significant advantage for improving the lifetime of the fuel cell system. A recent example of degradation-aware learning-based energy management is given in [17], where an enhanced soft actor-critic RL agent distributes the power demand among the stacks of a multi-stack fuel cell system depending on their individual state of health in order to avoid that the weakest stack limits the service life of the entire system.

Learning-based strategies (e.g., RL) require extensive historical data for the development of control strategies and are correspondingly computationally intensive [7,18]. They provide a solution close to optimality and are particularly suitable for multicriteria optimization problems [18]. However, LB strategies based on deep neural networks, such as RL, operate as so-called black box models: the internal decision-making process of the trained network is non-transparent and cannot be formally verified or traced back to physical quantities by engineers [19]. This opacity conflicts with automotive functional safety standards such as ISO 26262, which require formal verification and requirement traceability for safety-critical software in series production vehicle control units [20]. Currently, learning-based energy management strategies built on deep neural networks therefore have difficulty meeting the traceability and formal verification requirements of conventional

ISO 26262 functional safety, although the automotive industry is advancing safety standards, and implementation practices for functions based on artificial intelligence and interpretable RL approaches are being explored with regard to functional safety compliance.

Optimization-based (OB) algorithms regulate the control variables based on numerical computation results by minimizing a predefined cost function with feasible constraints [21]. According to [7], DP and Pontryagin's Minimum Principle (PMP) are the most frequently used global optimization algorithms. In [22], the DP for a FCEV is used to optimize the fuel cell power to reduce hydrogen consumption and extend the lifetime of the fuel cell. An optimal power distribution strategy for different degradation stages of fuel cells was derived in [23] using DP. Compared to a rule-based strategy, the operating costs of the fuel cell were reduced by 14.17% and the average lifetime was increased by 8.48%.

In [24] a health-conscious two-stage predictive energy management strategy for fuel cell electric heavy-duty long-haul trucks is proposed to overcome the challenges of durability and efficiency. The multi-objective optimization problem integrates component degradation as an inherent part of the optimization process to reduce the degradation of the battery and the fuel cell, taking into account the performance deterioration due to the progressive degradation of the powertrain components. To do so in the first stage, the fuel cell power and SoC profiles are optimized for the entire route once at the beginning of the driving cycle. The optimized references are followed by an on-board controller, representing the second stage of the predictive EMS, which is based on DP as an online EMS developed in [25].

For a fuel cell (FC) vehicle, ref. [26] combined optimal control using the PMP with a Markov chain model. The Markov chain prediction model was used to predict the future energy demand during the driving cycle. Another study used PMP as a global optimization method for the power distribution between the fuel cell and energy storage system in order to minimize hydrogen consumption [27]. Using a developed degradation model, a factor for limiting the fuel cell's power fluctuations with a weight coefficient was added to the PMP in [28] to increase the lifetime of the fuel cell. In comparison to an RB strategy, simulation results show a reduction of the fuel cell degradation by 56.4% in the China_city driving cycle, respectively, 57.8% in the Highway fuel economy test (HWFET) driving cycle. A similar strategy was used in [29] to limit fuel cell power fluctuations, extended by an SoC range limitation between 40% and 80%. As a result, dynamics of the fuel cell output could be reduced by 38.3% compared to a rule-based strategy.

OB-EMSs such as DP and PMP are able to find a global optimum for the given problem. The DP achieves the highest degree of optimality, but requires the highest computational effort and the longest computing time. The PMP approach can find a comparable optimum with a significantly lower computational cost. However, both strategies are mostly implemented offline due to higher computation requirements. Therefore, local optimization algorithms are primarily the focus for online implementation, as shown in [18,30].

Local optimization algorithms such as the Equivalent Consumption Minimization Strategy (ECMS), as well as Model Predictive Control (MPC) and stochastic dynamic programming (SDP), can find a local optimum close to the global optimal solution and can be implemented as real-time applications on control units.

The Equivalent Consumption Minimization Strategy (ECMS) is an online adaptation of the PMP algorithm where the global optimization problem is converted into a local problem.

Fuel consumption is specified as the optimization target in [31]. The total costs are made up of the equivalent cost of hydrogen consumption and the equivalent cost of the battery's electricity consumption. Since the driving profile is not known in advance, an equivalence factor correction function is used to adjust the SoC of the battery. Here, the actual equivalent factor is calculated by multiplying the SoC correction function by the

nominal equivalence factor. In [14], a two-stage ECMS is used to minimize the hydrogen consumption while protecting the proton exchange membrane fuel cell (PEMFC) at the same time. For this purpose in the first stage, a predictive controller is developed using the telemetry-equivalent consumption minimization strategy (T-ECMS) approach, which predicts the global optimality trend of the battery state of charge and the local control reference using telemetric driving information data. In the second step, a tracking controller is used that tracks the local control reference in the current control step to follow the optimal SoC reference, taking into account the PEMFC state constraints and other physical constraints. With the advancements in the availability of real-time information [21] presents a multi-layer predictive energy management with an ECMS in the lower layer combined with information such as live traffic data to reduce the fuel consumption. The proposed algorithm leads to a reduced fuel consumption in comparison to an RB strategy for a selected real-world use-case by 7.5%.

An ECMS can be easily implemented in real-time applications but have a lower adaptability for a fixed equivalence factor (EF). Their optimality is strongly dependent on the choice of EF and does not guarantee global optimality [18]. Adaptive ECMS (A-ECMS) can be used for online EF adaptation, providing local optimal solutions in real-time [32]. The real-time adaptation increases the complexity and thus the computing effort of the ECMS. Adaptive control at the converter level, such as the adaptive PI schemes in [12], addresses the tracking of a given power split rather than its optimality and is therefore complementary to, but not a substitute for, an adaptive supervisory EMS.

Model Predictive Control (MPC), also called Receding Horizon Control (RHC), is a global optimization algorithm that is applied as an online method for a finite time interval into the future, called the prediction horizon.

An EMS based on a linear MPC has been developed in [33] to improve battery performance and prevent fuel cell and battery degradation. Taking into account the different operating modes of the battery and the time constraints associated with the activation and deactivation of the fuel cell, an effort is made to maintain the discharge level of the battery at the optimal performance threshold and to minimize the hydrogen consumption. In order to reduce hydrogen consumption and improve the performance of the hybrid vehicle, Ref. [34] developed an MPC as a nonlinear constraint optimization problem to predict the optimal power of the fuel cell system in conjunction with prediction models for the future demand power for an FC vehicle. By using neural networks, improved results could be achieved for the optimization variables, in comparison to a Markov chain prediction model. However, neither strategy takes into account the aging of the fuel cell, except indirectly through operational constraints.

In the broader literature, fuel cell degradation is treated at different levels of detail depending on the application and the available information: (i) via operational constraints (e.g., limiting current/power gradients, avoiding start–stop events, and preventing operation in high-voltage or fuel-starvation regimes), (ii) via surrogate degradation metrics that can be embedded into an optimization objective (e.g., dynamic stress factors or voltage-decay-rate proxies), and (iii) via explicit state-of-health (SoH) states and deterioration-aware models that adapt the power split over the lifetime. In heavy-duty applications, experimental studies highlight the relevance of operating conditions for system efficiency and durability [35]. At the system-modeling level, map-based or efficiency-based representations are often used to enable integration into larger simulation frameworks, including other application domains such as aeronautics [36,37].

The different strategies are compared in terms of their optimality, computation time, degree of implementation, and real-time capability (see Figure 2).

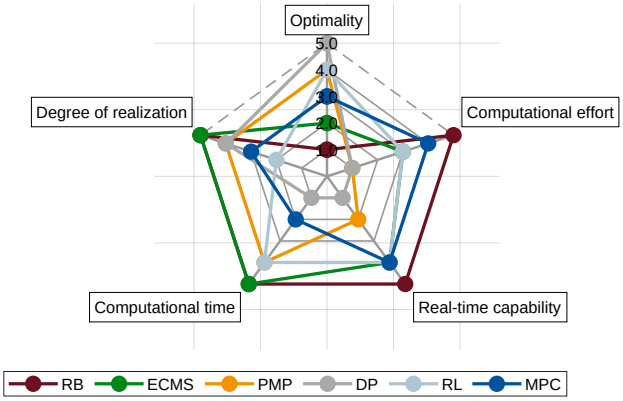


Figure 2. Comparison of the various operating strategies for FCEVs in terms of optimality, computing effort, real-time capability, computing time, and implementation effort (according to [38]).

Due to the ability to achieve a near-optimal solution to the DP with a high prediction horizon, as well as the consideration of system and control constraints, the chosen EMS for this work is the Model Predictive Control approach. To ensure real-time capability, the computational requirements of the MPC are solved using the advanced Acados solver [39,40].

1.2. Problem Definition

This work deals with the development of a model predictive control to optimize the energy efficiency of fuel cells, taking into account the lifetime of fuel cells. The described control strategy in [41,42] is used as a baseline strategy for the hybrid management as well as for the control of the fuel cell system. The contribution of this work with respect to existing literature is the formulation and real-time-capable implementation of a degradation-aware nonlinear MPC for a fuel cell heavy-duty vehicle, which (i) embeds a dynamic-operation degradation proxy directly into the optimal control problem (OCP) as an objective, (ii) jointly optimizes hydrogen consumption, system-efficiency-related terms, and fuel cell aging within a consistent constraint framework, (iii) is validated in a model-in-the-loop (MiL) environment on both a representative heavy-duty cycle (VECTO Long Haul) and a real driving cycle, with a comparison to both a global optimal DP benchmark as the upper bound of the achievable performance and a rule-based baseline without degradation awareness (Section 3.3), and (iv) can be implemented on automotive control units.

The paper is structured as follows: Section 2 describes the used simulation model for the FC heavy-duty vehicle (HDV), Section 3 delves into the development of the MPC. Section 4 provides a detailed analysis of the potential in hydrogen savings and the extension in lifetime of the fuel cell.

2. Simulation Model

In order to generate an accurate virtual representation of the real system, a detailed plant model in a MiL simulation is used, which is based on the modular fuel cell system simulation environment presented in [43]. The plant model can be divided into two main parts, one being the stack model and the other the system model, composed of the auxiliary components of the fuel cell system and the hybrid system.

Depending on the system structure, the components can differ greatly from one another, and therefore data maps are used to represent the different components. On the other hand, for the stack model [44], the approach is to use physical equations and a segmentation in the three spatial directions in order to achieve a high level of accuracy and account for local phenomena.

A visualization of the segmentation in the in-plane and through-plane directions of a stack cell is shown in Figure 3. On each side of a section in the through-plane direction, a bipolar plate is present through which the reaction gases and the coolant are fed. Further inwards there is additionally a section that represents the gas diffusion layer (GDL), which can be supplemented by a micro-porous layer (MPL) in order to model different types of fuel cells. In the middle, the cathode catalyst layer (CCL), the anode catalyst layer (ACL), and the membrane compose the membrane electrode assembly (MEA). For improved accuracy, the membrane and each GDL/MPL can be segmented into further parts, so that local phenomena can be modeled more precisely. The different effects taking place in the stack model can be separated into three distinct sections: mass transport, thermal dynamics, and electrochemistry.

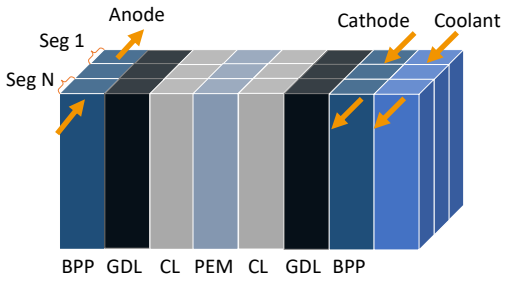


Figure 3. Segmentation of the cell in the in-plane and the through-plane direction.

The mass transportation is separated in the model in two distinctive parts. On the one hand, the movement of gases, such as oxygen, hydrogen, or nitrogen is considered. The transport mechanisms of water is modeled separately, as water molecules in the gas phase can change to the liquid condition depending on the conditions present in the system, and the two phases interact with each other. The motion of gas molecules can primarily be described by Knudsen diffusion, whereas liquid water is being transported through capillary pressure [45]. Moreover, the transport of water through the membrane is being considered. The distinction between sorption and desorption and the consideration of transient phenomena are particularly important in order to be able to better model the membrane behavior [46,47].

The thermal model considers the generated heat of the chemical reaction taking place at the cathode and the heat being generated through the transport of hydrogen ions being transported through the membrane and the electrons moving through the different cell components. The heat transfer in between the two bipolar plates is taken over by heat conduction, whereas convection is the primal force of the transfer from the gas channel material to the coolant. All effects of heat generation and transport are regrouped with the heat capacities of the different materials by a system of differential equations, which are solved to determine the temperature at various positions and at different points in time [45].

The calculated variables are used as an input for the electrochemistry model. Here, different effects are grouped together to determine the correct cell voltage. The theoretical cell voltage follows from the Nernst equation as a function of the local temperature and the partial pressures of hydrogen and oxygen in the gas channels; subtracting a constant voltage loss yields the open-circuit voltage (OCV). The activation losses are described by the Butler–Volmer equation, the ohmic losses by the electrical resistances of the cell components and the protonic resistance of the membrane, which depends on the membrane thickness δ_{mem} and the protonic conductivity, and the mass transport losses by the partial pressures of the reactants at the catalyst layers; activation and mass transport losses are evaluated separately for the anode and the cathode [48]. The underlying equations are standard and are not reproduced here; the modeling approach is described in detail in [44,45]. For the

evaluation of the energy management strategies, only the resulting cell voltage and the aging-related quantities of the stack model are relevant, which are introduced in Section 4.

The plant model described above serves as the virtual test bench of the MiL simulation, whereas the MPC uses a deliberately reduced prediction model, which is introduced in Section 3. Table 1 contrasts the two models, submodel by submodel. The reduction is dictated by the computing time available to the controller. The OCP is re-solved every 300 ms on the rapid control prototyping (RCP) hardware (Section 4.1) and is transcribed by direct multiple shooting on 400 shooting intervals (Section 3.2.1), so that every additional differential state of the prediction model enters all shooting nodes of the horizon, enlarges the quadratic subproblems of every sequential quadratic programming (SQP) iteration, and thus directly increases the solution time at every sampling instant. The segmented water, mass transport, and thermal dynamics of the plant model, which resolve each segment of the cell with its own set of differential states, are therefore not admissible in the prediction model, and the same applies to a thermal state of the battery. The prediction model is consequently restricted to the four states that are required to evaluate the objectives and constraints of the OCP, namely the SoC, the consumed hydrogen mass, the fuel cell power, and the cell voltage decay; all remaining submodels are represented by algebraic relations, i.e., the polarization curve, the balance-of-plant (BoP) characteristic, and the battery open circuit voltage and internal resistance as functions of the SoC. This reduction is admissible because the water and thermal states of the stack are regulated by subordinate control loops of the fuel cell control unit (FCCU): the coolant circuit controls the stack temperature, and the air path and the hydrogen supply control the humidification and the stoichiometry to their set points. From the perspective of the energy management, the fuel cell system therefore appears as a power source operated close to its nominal conditions, whose stationary behavior is captured by the polarization curve and by the BoP characteristic, both derived from steady-state operating points of the detailed plant model. The influence of the neglected water and thermal dynamics on the closed-loop result is nevertheless contained in the presented results, since the MPC is evaluated against the detailed plant model and not against its own prediction model.

Table 1. Comparison of the plant model used in the MiL simulation and the prediction model used inside the MPC.

Submodel	Plant Model (MiL)	MPC Prediction Model
Stack electrochemistry	Segmented physical model: Nernst voltage, activation, ohmic and mass transport losses evaluated with the local temperature and partial pressures [44,45]	0-D beginning-of-life polarization curve $U_{\mathrm{A,BoL}} = f(I_{\mathrm{St}})$ derived from steady-state operating points of the plant model; hydrogen mass flow from Faraday's law; no additional state
Water and mass transport	Gas transport (Knudsen diffusion), liquid water transport (capillary pressure) and water transport through the membrane (sorption/desorption)	Not modeled; nominal humidification implied by the polarization curve
Thermal behavior	Heat generation, conduction and convection to the coolant; temperature differential equations for each segment	Isothermal, no temperature state; electrical demand of the cooling system contained in the BoP characteristic
Balance of plant	Map-based component models of the auxiliaries (air path, coolant circuit, etc.), electrical demands summed up	Static characteristic $P_{\mathrm{BoP}} = f(I_{\mathrm{St}})$ from steady-state operating points of the plant model

Table 1. *Cont.*

Submodel	Plant Model (MiL)	MPC Prediction Model
Fuel cell degradation	Physics-based aging model for the electrochemically active surface area (ECSA) and the membrane thickness [49], integrated in the stack model (Section 4)	Empirical voltage-decay proxy U_{decay} driven by the dynamic-stress proxy σ (one state)
Battery	Electrical model with SoC- and temperature-dependent parameter maps coupled to a thermal model following [50,51]	Open circuit voltage and internal resistance as functions of the SoC, $T_{\text{bat}} = 25\,^{\circ}\text{C}$ constant; SoC as the only state
Electric drive and vehicle	Loss map of the electrical machine, constant efficiencies of inverter, gearbox and differential, longitudinal vehicle dynamics	Identical to the plant model

3. Methodology

The work follows the V-model for the development of control software, from the formulation of various requirements for the control model to system testing on an RCP control unit [52]. In the course of the development process, the FCCU with the MPC is implemented in the existing overall software, and the control functionalities are validated in a MiL environment before deploying it on the RCP control unit; the execution time measurements on the RCP unit are reported in Section 4.1.

The simulation environment consists of a control unit (CU) and a physical model, both implemented in `MATLAB Simulink` (R2021b) [53]. The control units of the individual components are coordinated by a higher-level control unit, the hybrid control unit (HCU). The input variables in the MPC are the driving profile information of the heavy-duty truck consisting of the velocity v, acceleration a and gradient profile α, a target SoC SoC_{ref} and the feed-back system state variables x. The result of the optimization problem is transferred to the system model in the form of an optimized power trajectory of the fuel cell, of which only the first step $u(0) = \Delta P_{\text{FCS}}(0)$ is applied as the fuel cell power request P_{FCS} before the OCP is re-solved with the updated state feedback. For a functioning control loop, the environment of the embedded system model must be simulated. For this purpose, the system model consisting of the battery, vehicle, and fuel cell is set up as a physical model within the MiL. An overview of the Optimal Control Problem (OCP) with the control constraints and the minimization objectives is shown in Figure 4.

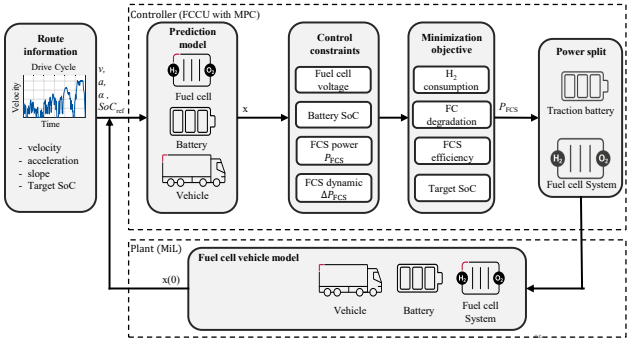


Figure 4. Optimal Control Problem (OCP) for minimization of hydrogen consumption and degradation of the fuel cell, with the signal flow between route information, controller and plant. The MPC receives the driving profile (v, a, α) and the reference SoC, predicts the states $x = (\text{SoC}, m_{\text{H}_2}, P_{\text{FCS}}, U_{\text{decay}})$ with the reduced prediction model subject to the constraints of Equation (39) and the objectives of Equation (42), and applies the first element $u(0) = \Delta P_{\text{FCS}}(0)$ of the optimal control sequence as the fuel cell power request P_{FCS} to the plant. The states are fed back from the plant model as the initial condition $x(0)$ at every sampling instant.

3.1. Models of the FCEV

The symbols used in the following model description and in the formulation of the OCP are summarized in the Nomenclature at the end of the manuscript. In particular, P_{FCS} denotes the net power of the fuel cell system, whereas P_{FC} denotes the gross power of the fuel cell stack.

3.1.1. PEMFC Model

The MPC model used for the description of fuel cell dynamics is a 0-D fuel cell model based on the polarization curve of the fuel cell. The characteristic curve is defined as the operating voltage over the operating current, with the voltage losses being deducted, and is set up in the form of an equation. The Nernst voltage U_{N}, also known as the OCV, is lower than the thermodynamically determined theoretical voltage value. Through a series of irreversible processes, the cell voltage is further reduced, resulting in the cell voltage U_{A}.

$$U_{\mathrm{A}} = U_{\mathrm{N}} - \Delta U \tag{1}$$

$$\Delta U = \Delta U_{\mathrm{Act}} + \Delta U_{\mathrm{Ohm}} + \Delta U_{\mathrm{Conc}} \tag{2}$$

The voltage losses can be considered to consist of activation overvoltage in combination with electrochemical limitations at the electrode surfaces ΔU_{Act}, ohmic losses in both the ionic and electronic conductors ΔU_{Ohm}, and concentration overvoltages at the electrodes during the reaction process ΔU_{Conc} [54]. By simplifying the fuel cell model using the polarization curve, the cell voltage $U_{\mathrm{A,BoL}}$ at the beginning of life (BoL) is approximated as a function of the stack current I_{St} resulting from the power demand P_{fc} of a single cell.

$$U_{\mathrm{A,BoL}} = f(I_{\mathrm{St}}) \tag{3}$$

$$I_{\mathrm{St}} = f(P_{\mathrm{FC}}) \tag{4}$$

The fuel cell efficiency η_{FC} related to the lower calorific value is the ratio of the net electrical system output P_{el} to converted chemical energy and includes the fuel mass flow $\dot{m}_{\mathrm{H_2}}$ and the lower calorific value of hydrogen $H_{\mathrm{u,H_2}}$.

$$\eta_{\mathrm{FC}} = \frac{P_{\mathrm{el}}}{\dot{m}_{\mathrm{H_2}} \cdot H_{\mathrm{u,H_2}}} = \frac{U_{\mathrm{St}} \cdot I_{\mathrm{St}}}{\dot{m}_{\mathrm{H_2}} \cdot H_{\mathrm{u,H_2}}} \tag{5}$$

The stoichiometric hydrogen consumption $\dot{m}_{\mathrm{H_2}}$ can be calculated using Faraday's law, where the molar mass of the hydrogen $M_{\mathrm{H_2}}$, the Faraday constant F and the electrochemical value z are used in the following equation:

$$\dot{m}_{\mathrm{H_2}} = \frac{M_{\mathrm{H_2}} \cdot P_{\mathrm{el}}}{z \cdot U_{\mathrm{A}} \cdot F} \tag{6}$$

The power of the auxiliary loads, consisting of the components described in Section 2, is determined as a function of the current fuel cell power. With an increase in the power demand on the fuel cell stack, there is a rise in the stack current, thereby determining the power of the BoP auxiliaries. The power output of the fuel cell system P_{FCS} is therefore the stack power P_{FC} minus the power of the auxiliary loads P_{BoP}.

$$P_{\mathrm{BoP}} = f(I_{\mathrm{St}}) \tag{7}$$

$$P_{\mathrm{FCS}} = P_{\mathrm{FC}} - P_{\mathrm{BoP}} \tag{8}$$

In this work, the BoP power is modeled at the system level as a static surrogate of the detailed plant model: the individual auxiliary consumers (air path, coolant circuit, etc.) are represented by map-based component models in the MiL plant, and their electrical power demands are summed up to obtain a total auxiliary power. For the EMS/MPC formulation,

this total is reduced to a one-dimensional characteristic $P_{\mathrm{BoP}} = f(I_{\mathrm{St}})$ (equivalently $f(P_{\mathrm{FC}})$), obtained from steady-state operating points of the detailed system model and implemented as a lookup table with interpolation. This choice keeps the OCP formulation simple and computationally efficient while still capturing the dominant trend that higher stack currents require higher auxiliary power.

In order to keep the degradation mechanisms of the fuel cell as low as possible, this work aims at a constant operation of the fuel cell with respect to the power output. Dynamic operation of the fuel cell leads to a high mechanical degradation of the fuel cell membrane and should therefore be avoided. In [55], a limitation of the voltage drop rate of the fuel cell is used to develop a strategy to protect against degradation. The aim of the strategy is to define an adaptive dynamic limit on the output power by formulating a relationship between the change in output power over time and the voltage drop rate. The drop rate $\frac{\partial u_{\mathrm{decay}}}{\partial t}$ is calculated based on Lin et al. [55] and Stevens et al. [56] using the following equation for each node k on the prediction horizon:

$$\frac{\partial u_{\mathrm{decay}}}{\partial t} = -\frac{225 \times \sigma[P_{\mathrm{FC}}(k) + \ldots + P_{\mathrm{FC}}(k-4)] + 10}{3600} \tag{9}$$

Experimental results in [55] show that the voltage drop rate under unit standard deviation σ of five consecutive power steps is 225 $\frac{\mu V}{h}$ in dynamic operation and 10 $\frac{\mu V}{h}$ in steady-state operation. The same approach was used to determine the drop rate in [56]. This is an empirical model for the effects of cyclic operation on the fuel cell degradation. According to [56], the degradation mechanisms caused by cyclic operation are mechanical wear of the membrane due to fluctuations in temperature and potential, and chemical degradation due to fluctuations in humidity and detachment of platinum particles at the cathode. The voltage drop rate calculates the decrease in the possible open circuit voltage using the standard deviation for five consecutive fuel cell power demands $P_{\mathrm{FC}}[k \ldots k-4]$. The MPC calculates the state variables based on the optimal control trajectory for the predicted time horizon into the future. The change in fuel cell power over the past five time steps cannot be stored in the MPC calculation and therefore cannot be used to calculate a standard deviation, as shown by Lin et al. [55] and Stevens et al. [56]. Alternatively, the change in fuel cell power between two consecutive time steps can be used as a dynamic-stress proxy that takes the place of the standard deviation in Equation (9). This proxy is not mathematically identical to the five-sample standard deviation; the consequences of this substitution for the empirical coefficient are discussed at the end of this section. Within the MPC, the proxy is defined as the normalized change in power from one time step to the next.

$$\sigma_{\mathrm{MPC}} = \frac{\left|\frac{P_{\mathrm{FC}}(k+1) - P_{\mathrm{FC}}(k)}{P_{\mathrm{FC,max}} - P_{\mathrm{FC,min}}}\right|}{2} = \frac{|\Delta P_{\mathrm{FC}}|}{2 \cdot (P_{\mathrm{FC,max}} - P_{\mathrm{FC,min}})} \tag{10}$$

Since the degradation is caused by the magnitude of the load change and not by its direction, Equation (10) is formed with the absolute value, as in the implementation, so that $\sigma_{\mathrm{MPC}} \geq 0$ and the decay rate of Equation (9) is negative for every power trajectory. The dynamic-stress proxy is zero in steady-state operation and reaches its maximum value of 0.5 for the largest admissible power change from $P_{\mathrm{FC,min}}$ to $P_{\mathrm{FC,max}}$ within one time step. The factor 1/2 in Equation (10) matches the value range of the proxy to that of the five-sample standard deviation of power values normalized to the interval $[0, 1]$, whose upper bound is approximately 0.5 as well. This means that the voltage drop can be estimated with the proxy and considered as an additional term within the cost function with respect to the degradation of the fuel cell system.

The actual cell voltage $U_{A,act}$ can be calculated from the continuous decrease in cell voltage over time using the following equation:

$$U_{A,act} = U_{A,BoL} + U_{decay}(t) \tag{11}$$

$$U_{decay}(t) = \int_{t_{BoL}}^{t} \frac{\partial u_{decay}}{\partial t} \cdot dt \tag{12}$$

The calculation of the decay rate can be used as a parameter to calculate the state of health (SoH) of the fuel cell. The SoH can be determined in the form of the following equation according to [56]:

$$SoH = 1 - \frac{U_{A,BoL} - U_A}{U_{A,BoL} - U_{A,EoL}} \tag{13}$$

Here, U_A denotes the current cell voltage and $U_{A,EoL}$ the cell voltage at end of life (EoL). Following [57], the EoL is reached as soon as the cell voltage at the rated operating point has dropped by 10% with respect to its value at the BoL:

$$U_{A,EoL} = 0.9 \cdot U_{A,BoL} \tag{14}$$

Substituting Equations (11) and (14) into Equation (13), the numerator becomes $U_{A,BoL} - U_{A,act} = -U_{decay}$ and the denominator $U_{A,BoL} - U_{A,EoL} = 0.1 \cdot U_{A,BoL}$, so that the SoH can be expressed directly in terms of the accumulated voltage decay.

$$SoH = 1 + \frac{U_{decay}}{0.1 \cdot U_{A,BoL}} \tag{15}$$

Since $U_{decay} \leq 0$ by definition of the negative decay rate, the SoH decreases monotonically from 1 at BoL to 0 at EoL. The SoH is not evaluated in Section 4; the aging assessment there is based directly on the membrane thickness and ECSA losses.

Transfer of the Empirical Decay Coefficient to the Proxy

The coefficient of 225 µV/h in Equation (9) was identified in [55] for the five-sample standard deviation and is applied to the proxy σ_{MPC} without recalibration. The two quantities differ: a single power change enters the standard deviation in all four windows that contain it, but the proxy only once. The dynamic share of U_{decay} computed with the proxy is therefore smaller than with the original relationship, and U_{decay} is to be read as a controller-internal measure of dynamic stress in the unit of a voltage, not as a calibrated prediction of the voltage decay.

This does not affect the results in Section 4. The coefficient enters the OCP only through the state equation of U_{decay}; power changes are penalized directly by σ in the cost vector of Equation (43), with a weight that is a calibration parameter of the vehicle configuration (Section 3.2.2). Rescaling the coefficient therefore leaves the penalty on power changes unchanged. Moreover, U_{decay} accumulates to only 13–14 µV over a complete drive cycle , most of it from the steady-state term of 10 µV/h. This is three orders of magnitude below the EoL threshold of $0.1 \cdot U_{A,BoL}$ in Equation (14). Finally, the aging assessment in Section 4 is based on the membrane thickness and ECSA losses of the physics-based aging model of the plant, which does not contain the coefficient. A re-identification of the coefficient for the proxy is required only if U_{decay} is to be used as a quantitative lifetime estimate, which is left for future work.

3.1.2. Vehicle Model

The driving resistance and the resulting power requirement of the vehicle are determined through longitudinal dynamics with the velocity, acceleration, and gradient profile of the driving cycles. The total driving resistance F_t is composed of various partial resistances:

$$F_t(t) = F_{air}(t) + F_r(t) + F_g(t) + F_a(t) \tag{16}$$

$F_{\text{air}}(t)$ is the aerodynamic resistance, which is based on the air friction on the vehicle surface and is given by

$$F_{air}(t) = \frac{1}{2} \cdot \rho_{\text{air}} \cdot A_{\text{proj}} \cdot c_{\text{w}} \cdot v(t)^2_{\text{act}} \tag{17}$$

where ρ_{air} is the air density, A_{proj} the projection area of the vehicle, c_{w} the aerodynamic drag coefficient, and v_{act} the current velocity.

The rolling resistance $F_{\text{r}}(t)$ is composed of the acceleration due to gravity g, the road slope angle α, the vehicle mass m_{v} and a constant rolling resistance coefficient f_{r}. It is calculated as follows:

$$F_{\text{r}}(t) = f_{\text{r}} \cdot m_{\text{v}} \cdot g \cdot \cos(\alpha) \tag{18}$$

$F_{\text{g}}(t)$ represents the grade force due to rthe oad slope, which is calculated as follows:

$$F_{\text{g}}(t) = m_{\text{v}} \cdot g \cdot \sin(\alpha) \tag{19}$$

The resistance due to acceleration $F_{\text{a}}(t)$ is calculated from the total mass m_{v} multiplied by the acceleration a_{v}:

$$F_{\text{a}}(t) = m_{\text{v}} \cdot a_{\text{v}}(t) \tag{20}$$

Multiplying the total drag force on the wheel F_{t} with the current vehicle velocity v_{act} results in the required power P_{t} at the wheel:

$$P_{\text{t}}(t) = F_{\text{t}}(t) \cdot v_{\text{act}} \tag{21}$$

The base vehicle and dimensioning are based on [42]. The specifications of the truck are given in Table 2:

Table 2. Vehicle specification.

Parameter	Symbol	Unit	Value
Vehicle weight	m_{v}	t	30
Tire specification	—	—	295/80 R22.5
Front surface	A_{proj}	m^2	9.7
Drag coefficient	c_{w}	—	0.53
Rolling coefficient	f_{r}	—	0.00467
Max. velocity	v_{max}	km/h	90

3.1.3. Electric Motor Model

The power of the electrical machine (EM) P_{em} can thus be determined via the efficiency chain, according to the following equation:

$$P_{\text{em}}(t) = \begin{cases} \frac{P_{\text{t}}}{\eta_{\text{dif}} \cdot \eta_{\text{gb}} \cdot \eta_{\text{inv}}} + P_{\text{em}_{\text{loss}}}, & P_{\text{t}} \geq 0 \\ P_{\text{t}} \cdot \eta_{\text{dif}} \cdot \eta_{\text{gb}} \cdot \eta_{\text{inv}} + P_{\text{em}_{\text{loss}}}, & P_{\text{t}} < 0 \end{cases} \tag{22}$$

where η_{dif} is the efficiency of the differential, η_{gb} is the efficiency of the gearbox and η_{inv} is the efficiency of the inverter.

The power loss of the electrical machine $P_{\text{em}_{\text{loss}}}$ is determined via a characteristic map as a function of the rotational speed n_{em} and the torque T_{em}. Using a third-degree polynomial function, the power loss can be approximated according to the following equation:

$$\begin{aligned} P_{\text{em}_{\text{loss}}} = {} & a_0 + a_1 \cdot n_{\text{em}} + a_2 \cdot |T_{\text{em}}| + a_3 \cdot n_{\text{em}} \cdot |T_{\text{em}}| \\ & + a_4 \cdot |T_{\text{em}}|^2 + a_5 \cdot n_{\text{em}} \cdot |T_{\text{em}}|^2 + a_6 \cdot |T_{\text{em}}|^3 \end{aligned} \tag{23}$$

The maximum drive power $P_{\text{prop}_{\text{max}}}$, which is composed of the power of the energy sources and the power for the auxiliary consumers, can be defined as follows:

$$P_{\text{prop}_{\text{max}}} = \eta_{\text{inv}} \cdot \left(P_{\text{bat}_{\text{max}}} + \left(P_{\text{FC,max}} - P_{\text{BoP}}\right) \cdot \eta_{\text{dcdc,Fc}}\right) \tag{24}$$

Here, $P_{\text{bat}_{\text{max}}}$ and $P_{\text{FC,max}}$ denote the maximum discharge power of the battery and the maximum power of the fuel cell stack, and $\eta_{\text{dcdc,Fc}}$ is the efficiency of the DC/DC converter that couples the fuel cell system to the HV bus.

3.1.4. Battery Model

For simplification, the focus is exclusively on the electrical battery model, as the thermal battery model is considerably more complex and challenging to represent due to the thermally dependent electrochemical processes [51,58]. In the electrical battery model, the voltage and the resulting current of a battery cell are calculated. The open circuit voltage of a battery cell u_{OCV} is determined based on the battery temperature T_{bat} and the *SoC* characteristic field and described in the form of a first-degree interpolated function for the purpose of simplification.

$$u_{\text{OCV}} = 3.262 + 0.892 \cdot SoC - 9.044 \cdot 10^{-18} \cdot T_{\text{bat}} \tag{25}$$

The battery temperature T_{bat} is considered constant and is set to 25 °C. In order to simplify the model, the thermal and transient temperature effects are neglected, since the battery model is now purely electric [50]. The only remaining state variable for the battery voltage is therefore the SoC. The high-voltage lithium-ion battery unit has an 186s3p configuration with a maximum capacity of 140 Ah and 98.84 kWh of energy. According to the specification, there are 186 cells connected in series $n_{\text{bat,ser}}$ and 3 parallel groups of cells $n_{\text{bat,par}}$. This results in the total battery voltage with open terminals U_{OCV} and the total capacity C_{bat} according to the following equations, with C_{cell} representing the capacity of a single battery cell:

$$U_{\text{OCV}} = u_{\text{OCV}} \cdot n_{\text{bat,ser}} \tag{26}$$

$$C_{\text{bat}} = C_{\text{cell}} \cdot n_{\text{bat,par}} \tag{27}$$

Following the subtraction of the internal resistance losses, the current battery voltage is determined. The loss voltage is contingent on the resulting current. In the following, $U_{\text{bat,act}}$ denotes the terminal voltage of the battery pack, $I_{\text{bat,act}}$ the actual pack current, which is positive for discharging and negative for charging, and R_{int} the internal resistance of the pack. The latter is composed of the cell resistances $R_{\text{int,dis}}$ for discharging and $R_{\text{int,chr}}$ for charging according to Equation (29), and $I_{\text{bat,act}}$ itself follows from the battery power via Equation (32).

$$U_{\text{bat,act}} = U_{\text{OCV}} - R_{\text{int}} \cdot I_{\text{bat,act}} \tag{28}$$

$$R_{\text{int}} = \begin{cases} R_{\text{int,dis}} \cdot \frac{n_{\text{bat,ser}}}{n_{\text{bat,par}}}, & I_{\text{bat,act}} \geq 0 \\ R_{\text{int,chr}} \cdot \frac{n_{\text{bat,ser}}}{n_{\text{bat,par}}}, & I_{\text{bat,act}} < 0 \end{cases} \tag{29}$$

The battery model has been reduced to a static equivalent circuit diagram, as illustrated in Figure 5.

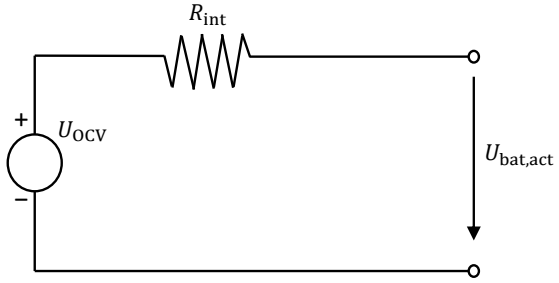


Figure 5. Electrical equivalent circuit diagram of the traction battery.

According to Hiseh et al. [59] and Geng et al. [14], the lithium-ion battery can be described by the internal electrical resistance model, using the following equation as a function of the voltage at the open terminals U_{OCV}, the internal resistance R_{int}, the power P_{bat} and the capacity of the battery C_{bat}.

$$\frac{\partial SoC}{\partial t} = -\frac{U_{OCV} - \sqrt{U_{OCV}^2 - 4 \cdot P_{bat} \cdot R_{int}}}{2 \cdot R_{int} \cdot C_{bat}} \tag{30}$$

From the relationship

$$SoC = SoC_0 - \frac{1}{C_{bat}} \int I_{bat,act}\, dt \tag{31}$$

with the initial state of charge SoC_0 gives the actual current of the battery:

$$I_{bat,act} = \frac{U_{OCV} - \sqrt{U_{OCV}^2 - 4 \cdot P_{bat} \cdot R_{int}}}{2 \cdot R_{int}} \tag{32}$$

The current battery power $P_{bat,act}$ is composed of the required power of the electric motor P_{em}, the supply power of the components of the fuel cell P_{BoP} and the electrical power supplied to the fuel cell P_{FC}.

$$P_{bat,act} = P_{em} - (P_{FC} - P_{BoP}) \cdot \eta_{dcdc,Fc} \tag{33}$$

The maximum charge power $P_{bat,min}$ and discharge power $P_{bat,max}$ of the battery depends on the battery temperature T_{bat} and the SoC. The map-based value can be approximated by a polynomial function for a battery temperature of 25 °C:

$$P_{bat,max} = f(SoC) \tag{34}$$

$$P_{bat,min} = f(SoC) \tag{35}$$

The parameters of the components used in this study are given in Table 3.

Table 3. Specification of the powertrain components.

Parameter	Symbol	Unit	Value
Electric machine peak power	$P_{em_{max}}$	kW	500
Max. motor speed	$n_{em_{max}}$	rpm	3400
Battery capacity	C_{bat}	kWh	98.84
Fuel cell System peak power	$P_{FCS,max}$	kW	303.6

3.2. MPC Energy Management Strategy

3.2.1. ACADOS Solver

`acados` (v0.4.5) [60] is an open source software package that provides a collection of solvers for optimization problems. `acados` is based on a powerful linear algebra library Blasfeo with an interface to `MATLAB` and `Python` and is designed for fast optimization in embedded applications [40]. It uses the SQP method to solve non-linear optimization problems (NOP). The Lagrange-Newton method for constrained problems with equation constraints is extended with inequality constraints and attempts to solve the optimization problem by iteratively solving quadratic approximations in the form of a linear Taylor approximation [61]. For this purpose, the Karush-Kuhn-Tucker (KKT) condition is used as an extension of the Lagrange method to solve the nonlinear optimization problem with inequality constraints and equation constraints.

3.2.2. Problem Formulation

To simplify the control problem, the change in fuel cell power is defined as the target variable. This has the advantages of avoiding excessive oscillations and of allowing the power gradient to be defined as a term within the cost function. The power of the battery is therefore equal to the difference between the power of the fuel cell and the power required by the powertrain and its consumers. The system input vector can be defined as follows:

$$u = (\Delta P_{\mathrm{FCS}}) \tag{36}$$

The state variables x consist of the SoC, the consumed hydrogen $m_{\mathrm{H_2}}$, the current fuel cell power output P_{FCS} and the cell voltage loss of the fuel cell U_{decay} of the dynamic system model:

$$x = \begin{pmatrix} \mathrm{SoC} \\ m_{\mathrm{H_2}} \\ P_{\mathrm{FCS}} \\ U_{\mathrm{decay}} \end{pmatrix} \tag{37}$$

The dynamic behavior of the system can be expressed as follows:

$$\dot{x} = \begin{pmatrix} -\frac{I_{\mathrm{bat,act}}}{C_{\mathrm{bat}} \cdot 3600} \\ \frac{P_{\mathrm{FC}} \cdot M_{\mathrm{H_2}}}{2 \cdot F \cdot U_{A,act}} \\ \Delta P_{\mathrm{FCS}} \\ -\frac{0.000225}{3600} \cdot \sigma - \frac{0.000010}{3600} \end{pmatrix} \tag{38}$$

The fourth row is the decay rate of Equation (9) in $\mathrm{V\,s^{-1}}$, evaluated with the dynamic-stress proxy σ from Equation (10). As discussed in Section 3.1.1, the empirical coefficients are used as identified in [55] and are not recalibrated for the proxy; within the OCP, U_{decay} acts as a bookkeeping state, while the penalty on dynamic operation is applied directly to σ in the cost function.

System constraints help to take into account boundary conditions resulting from safety aspects or physical limitations of control and state variables. Hard constraints are defined for the state and control variables in the form of inequalities whose limits must not be exceeded. The following constraints are defined for the state and control variables:

$$\begin{aligned} \mathrm{SoC}_{\mathrm{min}} \leq \mathrm{SoC} \leq \mathrm{SoC}_{\mathrm{max}} \\ 0 \leq m_{\mathrm{H_2}} \leq m_{\mathrm{H_2,max}} \\ P_{\mathrm{FCS,min}} \leq P_{\mathrm{FCS}} \leq P_{\mathrm{FCS,max}} \\ U_{\mathrm{decay,min}} \leq U_{\mathrm{decay}} \leq U_{\mathrm{decay,max}} \\ \Delta P_{\mathrm{FCS,min}} \leq \Delta P_{\mathrm{FCS}} \leq \Delta P_{\mathrm{FCS,max}} \end{aligned} \tag{39}$$

The SoC of the battery is limited to protect against overcharging or deep discharging and to protect against aging or performance degradation. The total hydrogen consumption is limited by the size of the tank. In addition to the physical limitation, hydrogen consumption is factored into the cost function and is therefore an optimization objective that should be minimized in the multivariable cost function with respect to minimum fuel consumption. Both the fuel cell and the battery have physical limits that must not be exceeded. A minimum power is defined as the lower limit for the fuel cell. This is to prevent the fuel cell from switching on and off and to prevent degradation. In the present configuration, the fuel cell system power is bounded to $P_{\mathrm{FCS,min}} = 25\,\mathrm{kW}$ and $P_{\mathrm{FCS,max}} = 303.6\,\mathrm{kW}$ and the battery SoC to $20\,\% \leq \mathrm{SoC} \leq 80\,\%$. The bounds $\Delta P_{\mathrm{FCS,min}}$ and $\Delta P_{\mathrm{FCS,max}}$ on the control input limit the power gradient of the fuel cell system. Since $u = \Delta P_{\mathrm{FCS}}$ enters the system dynamics

as the time derivative of P_{FCS}, these bounds are ramp-rate limits in kW s^{-1}. They are set to $\Delta P_{\mathrm{FCS,max}} = -\Delta P_{\mathrm{FCS,min}} = 100\,\mathrm{kW\,s^{-1}}$, corresponding to approximately one third of the rated system power per second. This value is derived from the dynamic response capability of the fuel cell system as represented in the plant model, in which the air path and the coolant circuit are modeled as dynamic components under the subordinate control of the FCCU (Section 2): within this limit, the power trajectory requested by the MPC can be followed by the air supply and the thermal management of the fuel cell system without cathode starvation or coolant temperature overshoot. The ramp-rate limit therefore reflects the load-change capability of the physical system rather than a tuning parameter, and it ensures that the fuel cell power request of the MPC is realizable by the subordinate FCCU without additional clipping. It is a hard constraint and must be distinguished from the dynamic-stress proxy σ in the cost function (see Equation (10)), which additionally penalizes power changes within the admissible range. A soft limit is defined for the cell voltage of a fuel cell:

$$U_{\mathrm{A,act}} \leq U_{\mathrm{A,max}} + \epsilon_1 \tag{40}$$

$$U_{\mathrm{A,act}} \geq U_{\mathrm{A,min}} - \epsilon_2 \tag{41}$$

The parameters ϵ_1, ϵ_2 allow the limits $U_{\mathrm{A,min}}$, $U_{\mathrm{A,max}}$ to be exceeded and are called slack variables. The slack variables appear within a term in the cost function and are penalized if the limit is exceeded. The purpose of limiting the cell voltage is to avoid excessively high and low voltages in the cell, which increase cell degradation. The admissible band is set to $U_{\mathrm{A,min}} = 0.55\,\mathrm{V}$ and $U_{\mathrm{A,max}} = 0.85\,\mathrm{V}$, and the slack variables are penalized quadratically.

The control and state variables to be optimized are combined as cost terms within the cost function, which is calculated as follows:

$$\begin{aligned} \min J(x(k), u(k)) = & \sum_{k=0}^{N_{\mathrm{p}}-1} (\beta(k)^{\mathrm{T}} \cdot Q \cdot \beta(k) \cdot Y) \\ & + \sum_{k=0}^{N_{\mathrm{p}}-1} \left(\frac{1}{2} \cdot \epsilon^{\mathrm{T}} \cdot G \cdot \epsilon \right) \\ & + \left(A \cdot (\mathrm{SoC}(N_{\mathrm{p}}) - \mathrm{SoC}_{\mathrm{ref}}(N_{\mathrm{p}}))^2 \cdot W \right) \end{aligned} \tag{42}$$

with

$$\beta(k) = \begin{pmatrix} \dot{m}_{\mathrm{H_2}}(k) \\ \sigma(k) \\ 1 - \eta_{\mathrm{ec,Fc}}(k) \\ u(k) \end{pmatrix} \tag{43}$$

The cost function can be roughly divided into three terms. The first term is the vector $\beta(k)$ describing the objectives to be minimized within the cost function at each time step within the horizon H for the nodes $k = 0 \ldots N_{\mathrm{p}-1}$. Its four elements are the hydrogen mass flow $\dot{m}_{\mathrm{H_2}}$ from Equation (6), the dynamic-stress proxy σ from Equation (10), the electrochemical efficiency deficit $1 - \eta_{\mathrm{ec,Fc}}$ and the control input u. The electrochemical efficiency $\eta_{\mathrm{ec,Fc}} = U_{\mathrm{A,act}}/U_{\mathrm{rev}}$ is the ratio of the actual cell voltage from Equation (11) to the reversible cell voltage $U_{\mathrm{rev}} = 1.229\,\mathrm{V}$; in contrast to the system efficiency η_{Fc} in Equation (5), it depends only on the predicted cell voltage and thus penalizes operation at low cell voltage, i.e., at high current density, directly within the prediction model. The second term is the penalty for exceeding the cell voltage limits of a fuel cell, and the third term is the deviation of the SoC from a reference SoC value at the end of the horizon $k = N_{\mathrm{p}}$ as the terminal cost. Since only the SoC is given as a reference, this term describes the deviation of the

SoC from the reference SoC. The matrices Q, Y and the variables A, W are responsible for factorizing and weighting of the respective terms within the cost function. The weights, together with the SoC operating band, are calibration parameters: they encode the trade-off between hydrogen consumption, fuel cell degradation, and charge sustaining and are therefore specific to the vehicle configuration and the operator's preference. In contrast to the physical constraints in Equation (39), their numerical values are not transferable to another system and are not reported as such. All strategies in Section 4 were tuned for the same vehicle configuration and the same SoC target of $\mathrm{SoC}_{\mathrm{ref}} = 60\,\%$. The calibration parameters of all strategies, i.e., the weights of the MPC cost function, the corresponding parameters of the DP, and the gain of the rule-based strategy, were tuned on the VECTO Long Haul cycle only. The Aachen-Eifel real driving cycle serves as a transfer and validation case: it was simulated with the identical parameter sets, without any recalibration, so that the results on this cycle show whether the calibration obtained on VECTO transfers to a real driving profile that was not used for tuning.

Solution Procedure

The OCP defined by Equations (39) and (43) is solved at every sampling instant of the MPC by the SQP algorithm described in Section 3.2.1. The solution procedure is summarized as follows. (i) Discretization: the continuous-time OCP is transcribed by direct multiple shooting on N_{p} equidistant shooting intervals of 1 s over the prediction horizon H, so that $N_{\mathrm{p}} = H/1\,\mathrm{s}$; the horizon length is selected in Section 4.1. The system dynamics are integrated on each interval with an explicit fourth-order Runge–Kutta scheme (ERK, one integration step per interval). The driving profile information (acceleration, velocity, and gradient) enters as a parameter vector $p(k) = (a_{\mathrm{veh}}, v_{\mathrm{veh}}, \alpha)$ at each shooting node. (ii) Cost and constraints: the cost function is implemented as an external quadratic cost with the elements of $\beta(k)$ as residuals, the cell voltage limits as soft nonlinear path constraints with quadratically penalized slack variables, and the state and input bounds as hard box constraints. (iii) SQP iteration: starting from the solution of the previous sampling instant (warm start), at most ten full-step SQP iterations are performed per sampling instant, using a Gauss–Newton Hessian approximation. Each quadratic subproblem is solved with the interior-point quadratic programming (QP) solver HPIPM [40]. The iteration is terminated when the KKT residuals of stationarity, equality, inequality, and complementarity fall below 10^{-6} or when the iteration limit is reached; in the latter case the current iterate is applied, and the computing time analysis in Section 4 confirmed that the iteration limit was not active with the selected horizon. (iv) Application: only the first element $u(0) = \Delta P_{\mathrm{FCS}}(0)$ of the optimal control sequence is applied; the resulting fuel cell power setpoint is transmitted to the FCCU as the power request of the fuel cell system. (v) Receding horizon: at the next sampling instant, the current states SoC, $m_{\mathrm{H_2}}$, P_{FCS} and U_{decay} are fed back from the plant as the initial condition $x(0)$, the parameter trajectory is shifted along the driving profile, and steps (iii)–(iv) are repeated. The solver is generated as C code and embedded in `Simulink` (R2021b) [53] as an S-function, so that the same code base is used in the MiL environment and can be compiled for the target control unit.

3.2.3. Drive Cycles

The VECTO Long Haul cycle is a driving cycle for determining the CO_2 emissions and the fuel consumption of heavy-duty commercial vehicles. It is derived from the European Commission's Vehicle Energy Consumption Calculation Tool (VECTO) [62]. The cycle represents a typical truck driving profile with constant speed sections and few start-stop operations over a distance of approximately 100 km with uphill and downhill gradients

at a maximum speed of up to 87.5 km/h. Figure 6 shows the driving profile information consisting of acceleration, velocity and gradient profile over the cycle time.

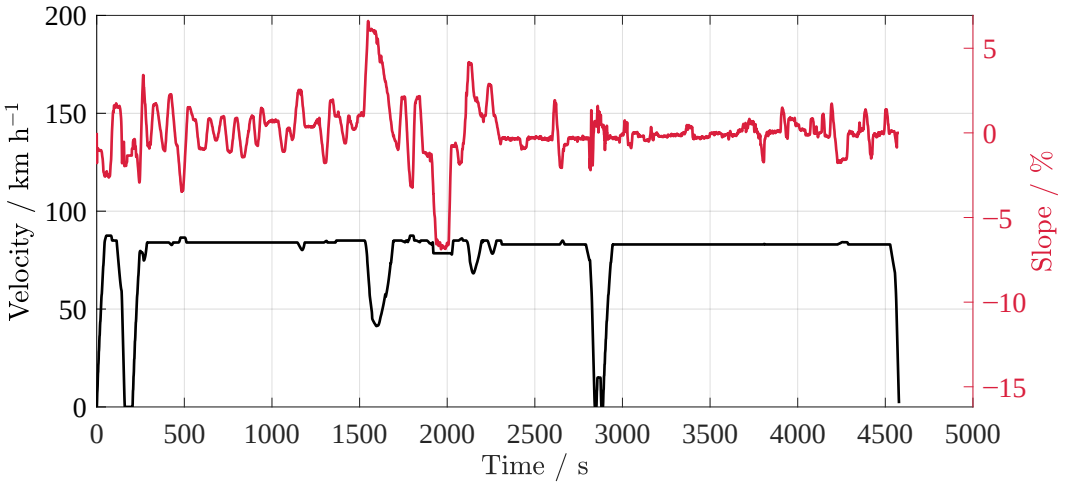


Figure 6. VECTO Long Haul drive cycle velocity and slope profile (distance approx. 100 km, average speed 78 km/h, maximum speed 87.5 km/h).

Another cycle used to validate the MPC is a real-world driving cycle on rural roads from the city of Aachen through the Eifel region, referred to as the Aachen-Eifel real driving cycle in the following. The Eifel is an area in North Rhine-Westphalia, Germany, which provides an interesting cycle for comparing the MPC with the DP due to its dynamic elevation and velocity profile. The velocity, and gradient profile over the cycle time is shown in Figure 7.

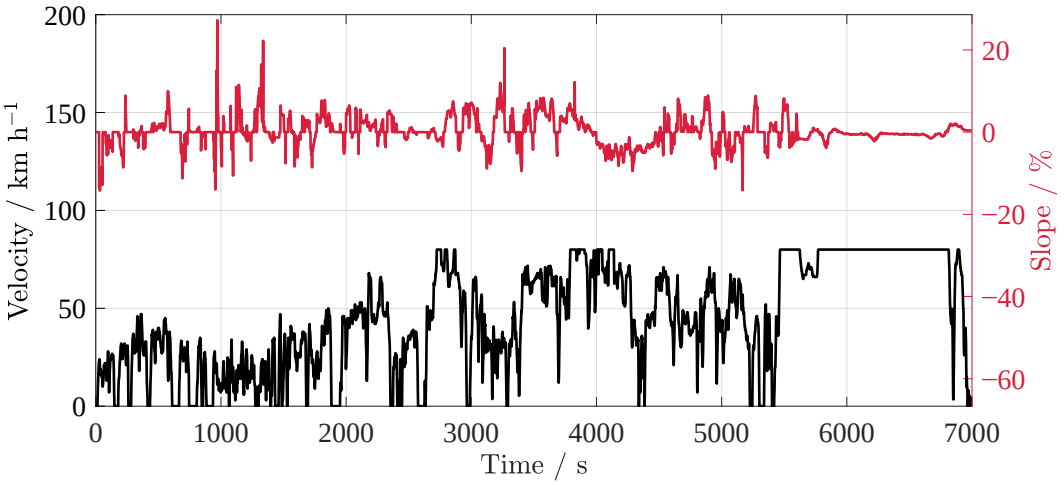


Figure 7. Aachen-Eifel real driving cycle velocity and slope profile (distance approx. 87 km, average speed 45 km/h, maximum speed 80 km/h).

3.3. Rule-Based Baseline Strategy

The rule-based (RB) strategy used as the baseline in Section 4 splits the electrical load demand P_{em} between the fuel cell system and the HV battery by a fixed proportional control law. The fuel cell power setpoint follows the load demand, corrected by a term proportional to the SoC error with the gain K_{SoC}, and is saturated to the same admissible range $[P_{\text{FCS,min}}, P_{\text{FCS,max}}]$ as in the MPC (Equation (39)); the battery covers the remaining difference within its power limits:

$$P_{\mathrm{FCS}} = \min\Big(\max\left(P_{\mathrm{em}} + K_{\mathrm{SoC}}\left(\mathrm{SoC}_{\mathrm{ref}} - \mathrm{SoC}\right), P_{\mathrm{FCS,min}}\right), P_{\mathrm{FCS,max}}\Big), \qquad P_{\mathrm{bat}} = P_{\mathrm{em}} - P_{\mathrm{FCS}}. \tag{44}$$

If the SoC is below its reference, the fuel cell is driven to a higher power and charges the battery; if it is above, the fuel cell power is reduced accordingly. The gain K_{SoC} is a calibration parameter that has to be tuned specifically for the vehicle configuration and the expected load profile. Once set, it is fixed: the RB strategy cannot adapt its power split to the actual driving situation, and a gain that provides acceptable charge sustaining on one profile may cause the SoC to overshoot its target or the fuel cell to operate unnecessarily dynamically on another. In this work, K_{SoC} is kept identical for both drive cycles. In contrast to the MPC, no trade-off between hydrogen consumption, battery usage, and fuel cell degradation is performed, and the degradation of the fuel cell is not considered at all. The RB strategy therefore serves as the reference for a control law without degradation awareness, whereas the DP provides the upper bound of the achievable performance with full knowledge of the driving profile.

4. Results

The fuel cell degradation reported in this section is calculated by an ECSA aging model integrated into the stack model described in Section 2, following established literature on ECSA aging [49,63–65]. Within the MPC cost function, a cyclic-operation-induced voltage decay is represented by the state U_{decay}, obtained by integrating the empirically parameterized decay rate (see Equation (12)) with the dynamic-stress proxy σ (see Equation (10)), so that the effect of power fluctuations on the voltage loss is directly penalized during optimization. The resulting end-of-cycle degradation is evaluated through two complementary indicators based on the aging model from Thiele et al. [49]: the relative membrane thickness change ($\Delta\delta_{\mathrm{mem}}$) and the relative electrochemically active surface area loss (ΔA_{ECSA}). The results are deliberately reported as relative values only. The parameters of the aging model are taken from the literature and have not been validated against measurements of the stack considered here, so the absolute magnitudes of the degradation over a single drive cycle are not considered robust. Since all three strategies are evaluated with the identical plant and aging model on the identical driving profile, the relative comparison isolates the influence of the energy management strategy, which is the objective of this study. While the absolute changes over a single drive cycle are small, the comparison highlights a consistent trend: the highly dynamic RB strategy leads to the largest degradation in both indicators and on both cycles, whereas the MPC attains the lowest membrane thickness loss and stays close to the globally optimal DP in terms of ECSA loss on the VECTO cycle, which is consistent with the objective of smoothing the fuel cell power trajectory.

The relation between the macroscopic proxy in the controller and the microscopic degradation indicators of the plant deserves clarification. The MPC does not contain any mechanistic degradation model: σ and U_{decay} quantify the dynamic stress of the fuel cell power trajectory and penalize it in the cost function, without any statement about individual degradation mechanisms. The membrane thickness and ECSA results reported in this section are, in contrast, computed by the physics-based aging model of the segmented stack model in the plant [49], which evaluates the local operating conditions of each segment and is entirely independent of the controller proxy. The plant model thus provides an independent evaluation of the proxy: the degradation indicators are obtained from a mechanistic model in which σ does not appear, so that any reduction of membrane thinning or ECSA loss achieved by the controller results from the effect of the penalized power dynamics on the local operating conditions of the stack, not from the proxy itself. The physical link between the two levels is well documented, as load cycling is identified as one

of the dominant lifetime-limiting factors of automotive PEMFC stacks and is associated with mechanical fatigue of the membrane through fluctuations of temperature, humidity, and potential as well as with the detachment and dissolution of platinum particles at the cathode [56,66,67]. Consistently, the most dynamic RB strategy exhibits the highest degradation in both indicators on both cycles. The mapping is, however, not complete. The differences between the MPC and the DP are dominated by the operating voltage level rather than by its fluctuation (see the discussion of the degradation results in Section 4.4), and voltage-level-dependent pathways such as peroxide-induced membrane degradation and platinum dissolution at high potentials are not represented by σ. The proxy therefore captures the dynamic-operation-induced share of the degradation, which is the share the energy management strategy can influence, whereas the comparison of the indicators between the strategies is always made with the mechanistic plant model.

4.1. Computing Time Analysis

In order to evaluate how the length of the prediction horizon H affects the computation time and the optimality of the results, a variation of the horizon lengths is performed and analyzed. Previously, the change in execution time t_{CPU} was investigated by varying the maximum iteration steps, with the result that the optimum solution was achieved within the defined maximum SQP iteration steps in each computation step, so this consideration is ignored. For this purpose, a cycle similar to the VECTO Long Haul cycle is evaluated within the MiL for a horizon range of 50–1000 s. The considered execution time t_{CPU} is the total execution time of the S-function of the OCP in `Simulink` per sample time (Windows 10 desktop PC with an Intel Xeon W-2123 (Intel Corporation, Santa Clara, CA, USA) at a clock speed of 3.6 GHz and 64 GB RAM). The maximum computation value occurring within the entire cycle is used as the reference value for the analysis, as this value is more meaningful in terms of execution on an electronic control unit. The choice of prediction horizon has a direct influence on the execution time of the MPC. As the horizon increases, the optimum performance trajectory for each grid point is calculated for that period into the future. To quantify this influence, the cycle was run with the horizon lengths:

$$H \in \{50\,\mathrm{s},\ 100\,\mathrm{s},\ 200\,\mathrm{s},\ 300\,\mathrm{s},\ 400\,\mathrm{s},\ 500\,\mathrm{s},\ 600\,\mathrm{s},\ 800\,\mathrm{s},\ 1000\,\mathrm{s}\} \tag{45}$$

Figure 8 shows the progression of the target variables as a function of the horizon length of the MPC. It can be seen that the maximum execution time increases as the horizon length increases. The maximum execution time at 500 s and 600 s falls out of the pattern and is less than the execution time at 400 s. From a horizon length of 800 s, the maximum permissible execution time of 300 ms is exceeded. This limit corresponds to the task rate at which the MPC S-function is scheduled within the FCCU software, i.e., the OCP is re-solved every 300 ms, while the plant and the remaining controller functions run in a 10 ms base task; the two rates are coupled by rate transition blocks. If executed on a controller, the MPC would run into task overruns, which must be avoided. The average execution time increases only slightly with increasing horizon length, but the cell voltage loss decreases significantly with increasing horizon length. At horizon lengths below 200 s the gradient of the cell voltage loss is significantly higher, thus, with regard to the cell voltage loss, a horizon length of at least 200 s should be chosen. It can be seen that a horizon length of 400 s reflects a good compromise between the lowest possible maximum execution time, low fuel consumption, low deviation from the target SoC and cell voltage loss. As a result of this parameter analysis, a prediction horizon of 400 s is selected for further investigation.

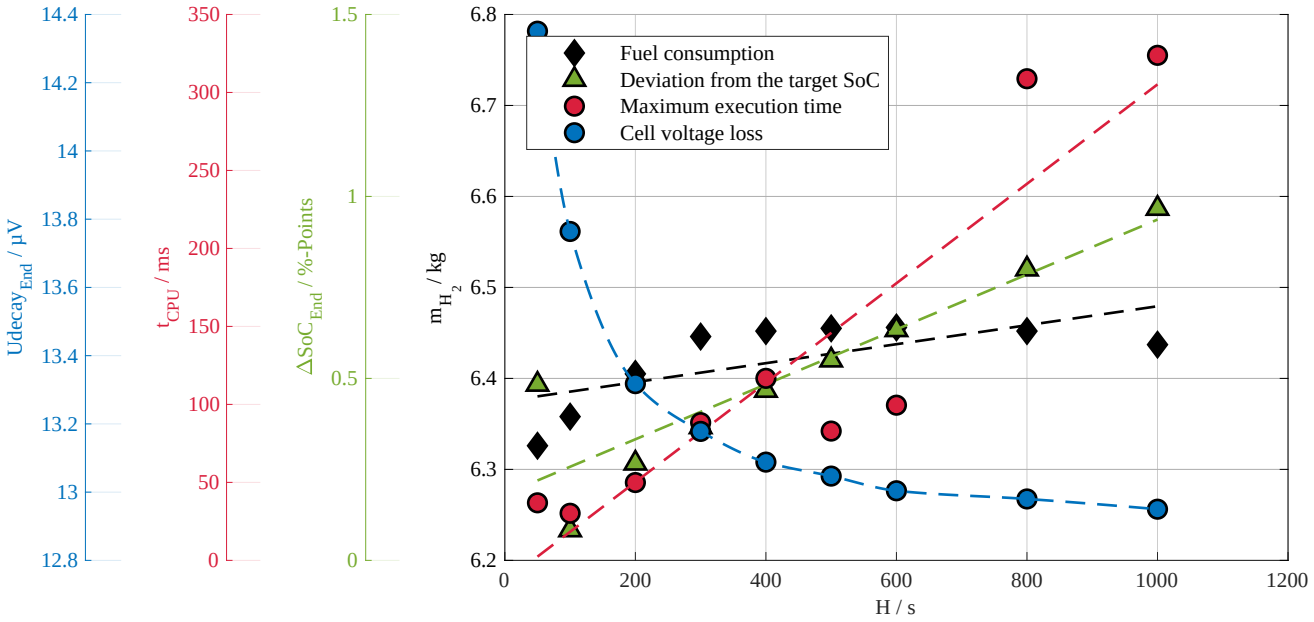


Figure 8. Effect of varying the prediction horizon length H on the deviation from the target SoC, fuel consumption, cell voltage loss, and the maximum execution time of the MPC.

Execution on Rapid Control Prototyping Hardware

The execution times discussed above were measured on the desktop PC of the MiL environment. To verify the real-time capability on embedded hardware, the complete `Simulink` model, consisting of the control model including the FCCU with the MPC and the plant model, was additionally compiled for and executed on a MicroAutoBox III RCP unit (dSPACE GmbH, Paderborn, Germany) (DS1403 platform, Texas Instruments AM5K2E04 with four ARM Cortex-A15 cores at 1.4 GHz and 2 GB RAM) [68]. For this purpose, the `acados` libraries were cross-compiled for the target with the dSPACE CMake toolchain and linked to the generated S-function as custom code. The application runs in two task rates, the 10 ms base task of the plant and controller models and the 300 ms MPC task. On the VECTO Long Haul cycle with the selected prediction horizon of 400 s and the solver settings of Section 3.2.1, the base task required 16.7 µs on average and 45.5 µs at maximum. The MPC task required 158.2 ms on average, with increasing computing time towards the end of the cycle, where the upper bound of the fuel cell power is ramped down towards $P_{\mathrm{FCS,min}}$ for the shooting nodes beyond the end of the cycle in order to prepare the shutdown of the fuel cell system. The tightened bounds increase the number of SQP iterations required for convergence, and the 300 ms task was exceeded in this phase when the iteration limit became active. The fuel cell power and SoC trajectories obtained on the RCP unit coincide with those of the MiL simulation.

The RCP measurements therefore confirm that the MPC with the selected horizon is executable within the 300 ms task on embedded hardware for the entire. Measures to reduce the execution time towards the end of the cycle without shortening the prediction horizon are relaxing the KKT tolerance, reducing the maximum number of SQP iterations towards a real-time iteration scheme, executing the MPC on a dedicated core of the RCP unit, and removing the end-of-cycle power limitation. These measures and the subsequent hardware-in-the-loop validation with the FCCU on the MicroAutoBox III and the plant model on a dSPACE SCALEXIO system [69] are the subject of ongoing work.

4.2. MPC vs. DP

4.2.1. VECTO Long Haul Cycle

In the following, the model predictive control approach is compared to a DP with respect to its optimality. The DP is designed to compute an optimal SoC trajectory, taking into account the minimum fuel consumption and the rate of change in fuel cell system power. The same boundary conditions and performance constraints are applied to both the MPC and the DP in order to compare the results. Due to the deviation of the mathematical system model in the MPC and DP from the simulation model in the MiL environment, a balanced state of charge at the end of the driving cycle cannot be guaranteed. In order to be able to guarantee the comparability of the consumption results, nevertheless, the charge deviations in fuel consumption must be taken into account. A correction is therefore applied in both directions, so that all strategies are evaluated at an identical, balanced charge level at the end of the cycle. In the case of a positive charge deviation ($\mathrm{SoC_{end}} < \mathrm{SoC_{start}}$), the energy missing in the battery is converted into an additional fuel mass to be applied, taking into account the overall efficiency, so that no artificial fuel consumption advantage is created. Conversely, in the case of a negative charge deviation ($\mathrm{SoC_{end}} > \mathrm{SoC_{start}}$), which can occur, for example, due to extended recuperation during downhill driving, the surplus energy remaining in the battery is credited as an equivalent fuel mass and deducted from the consumption. Both cases are covered by the same correction rule formulated in [70] according to equation

$$m_{\mathrm{H_2,cor}} = m_{\mathrm{H_2,end}} + \frac{(\mathrm{SoC_{start}} - \mathrm{SoC_{end}}) \cdot (-C_{\mathrm{batt}})}{\eta_{\mathrm{Fc}} \cdot \eta_{\mathrm{inv}} \cdot \eta_{\mathrm{bat}}} \cdot \frac{1}{H_{\mathrm{u,H_2}}} \tag{46}$$

which adjusts the fuel mass $m_{\mathrm{H_2,end}}$ determined from the simulation as a function of the charge difference. For the fuel cell system efficiency η_{Fc} an average efficiency from the drive cycle is used. The overall efficiency is the efficiency of the electrical path and includes the fuel cell, the inverter, and the battery.

The fuel cell system power and state of charge (SoC) trajectories of DP and MPC in the MiL environment using the gradient and speed profile for the VECTO Long Haul cycle are compared in Figure 9. The DP controller maintains a nearly constant fuel cell power of about 95 kW, which is close to one-third of the fuel cell's maximum power and therefore in the range of the best efficiency point for fuel cell system operation. The power trajectory of the MPC, on the other hand, is considerably more dynamic and varies between a minimum of about 25 kW and a maximum of about 217 kW. These differences in power trajectories also affect the SoC trajectories. The DP allows a wider range of SoC to be covered compared to the MPC due to its knowledge of the entire driving profile.

Within the prediction horizon $H = 400\,\mathrm{s}$, the MPC searches for the optimal fuel cell power from which the SoC trajectory is derived. It tries to achieve the target SoC at the end of the horizon, which is reflected in the maximum deviation of the SoC within the prediction horizon. The SoC of the DP reaches its minimum at $t = 1770\,\mathrm{s}$ and drops to a value of about 41%. The DP thus uses 34% of the allowed SoC operating range (i.e., the permissible SoC band between $\mathrm{SoC_{min}}$ and $\mathrm{SoC_{max}}$). The SoC of the MPC reaches its minimum of 51% at $t = 1692\,\mathrm{s}$ and its global maximum of 66.8% at $t = 2094\,\mathrm{s}$, thus using 26% of the allowed SoC range. From the results obtained, a SoC deviation from the desired target SoC can be determined for both the MPC and the DP. The MPC misses the target SoC by −1.06% and has a state of charge of 59.4% at the end of the cycle, while the DP ends at a state-of-charge of 60.6%, i.e., 0.93% above the target SoC. After correcting the fuel consumption for the state of charge deviation at the end of the cycle, the fuel consumption for the MPC is 7.18 kg. With a fuel consumption of 6.97 kg, the globally optimal DP control therefore consumes 2.9% less hydrogen than the MPC control.

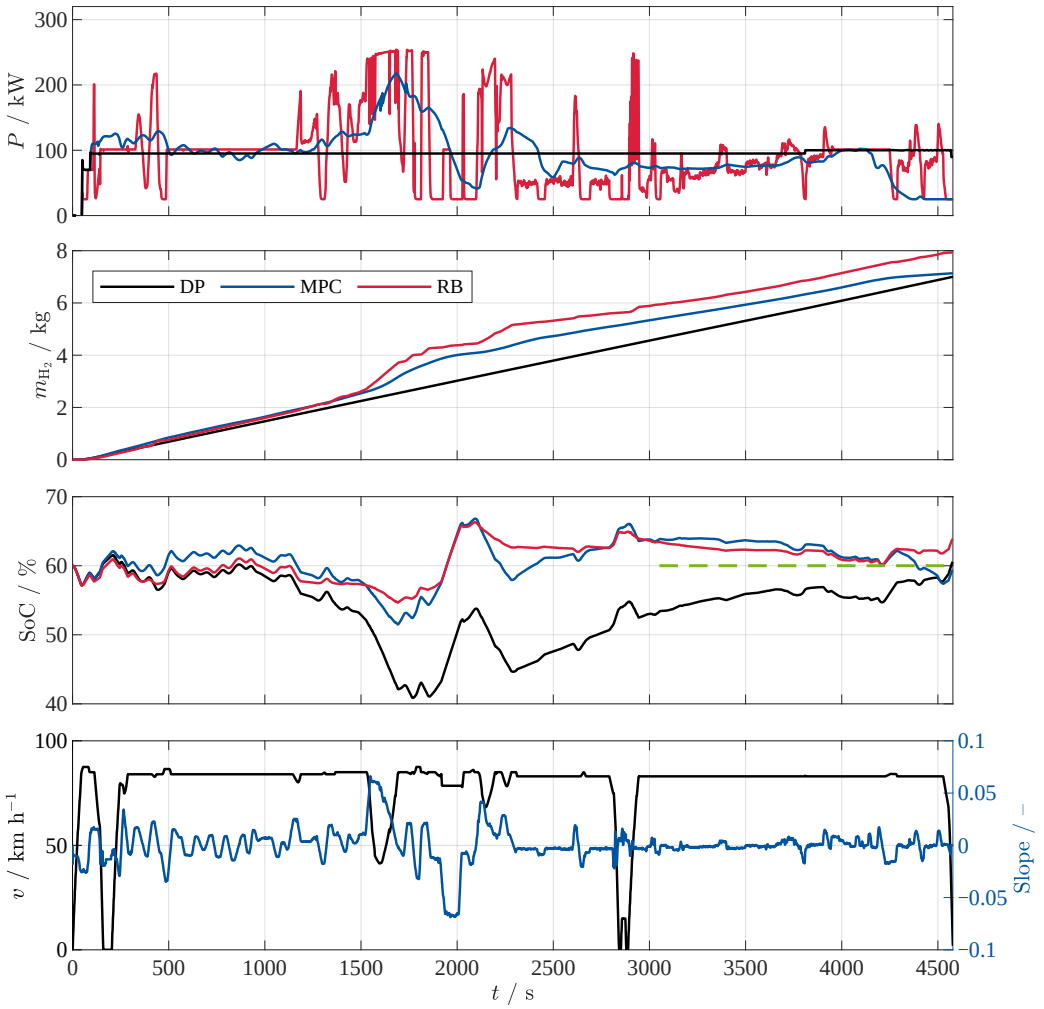


Figure 9. Comparison of the FC system power trajectory and the SoC trajectories between the DP, MPC, and RB control (prediction horizon 400 s) in the MiL environment with the gradient and speed profile of the VECTO Long Haul cycle. While the DP tries to maintain the target SoC only at the end of the cycle, the MPC tries to achieve the target SoC at the end of each horizon.

4.2.2. Aachen-Eifel Real Driving Cycle

Figure 10 shows a comparison between the FC system power trajectories and the SoC trajectories of DP and MPC in a MiL environment using the gradient and speed profile of the Aachen-Eifel real driving cycle over time. The main difference between global and local optimal control is evident in the SoC power trajectories. The DP control, which benefits from global information about the driving profile, mostly performs in the range of optimal efficiency and minimum fuel consumption, similar to the VECTO Long Haul cycle. However, the DP control mostly operates in a narrow band between about 55 kW and 65 kW, with isolated peaks up to 95 kW due to the influence of the gradient and speed profile.

Unlike the MPC, the DP detects the high-speed section at the end of the cycle and charges the battery more initially, reaching a maximum SoC of 75.4% at $t = 1755$ s before drawing it down to a minimum of 29.1% at $t = 4006$ s. As a result, the DP regulates a more constant fuel cell power output throughout the cycle to maintain low hydrogen consumption and high efficiency. On the other hand, the MPC reaches a global maximum SoC of 73.1% at $t = 4385$ s. Due to its limited knowledge of the driving cycle information according to the defined finite time horizon, the power output of the MPC differs from the power output of the DP, resulting in a more dynamic trajectory and a maximum power of 244 kW at

$t = 3865$ s. The DP uses a substantially larger part of the allowed SoC range (77%) compared to the MPC (43%). The final SoC of the DP control is 59.9%, which is 0.2% below the target SoC, and the final SoC of the MPC control is 63.6%, which is 6.1% above the target SoC. With respect to the total hydrogen consumption, the advantage of the global optimality of the DP is clearly visible. After correcting the charge deviation for the MPC and DP control to the target SoC, the total hydrogen consumption of the MPC is 7.65 kg, which is 10.7% higher than the DP's consumption of 6.91 kg. The corrected hydrogen consumption of the DP, MPC, and RB strategies for both drive cycles is summarized in Figure 11a,b.

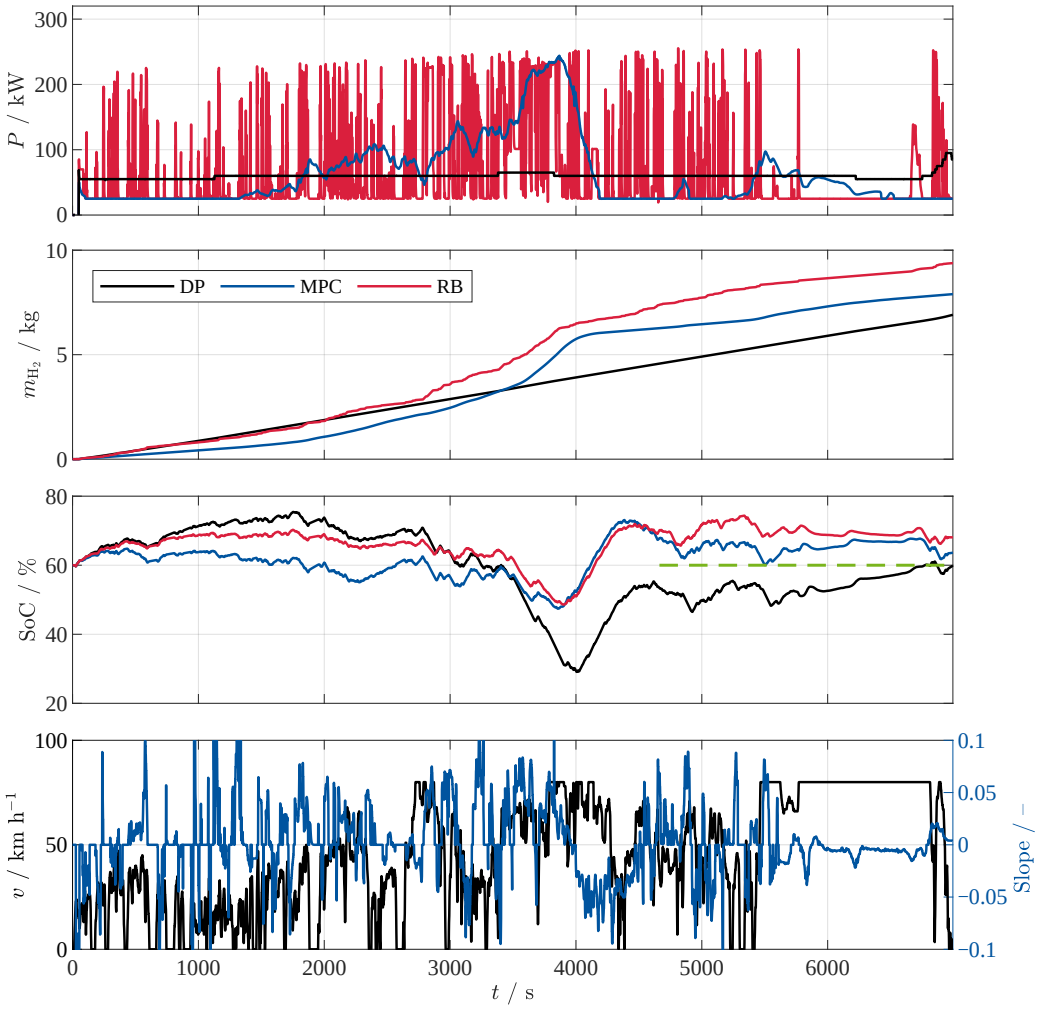
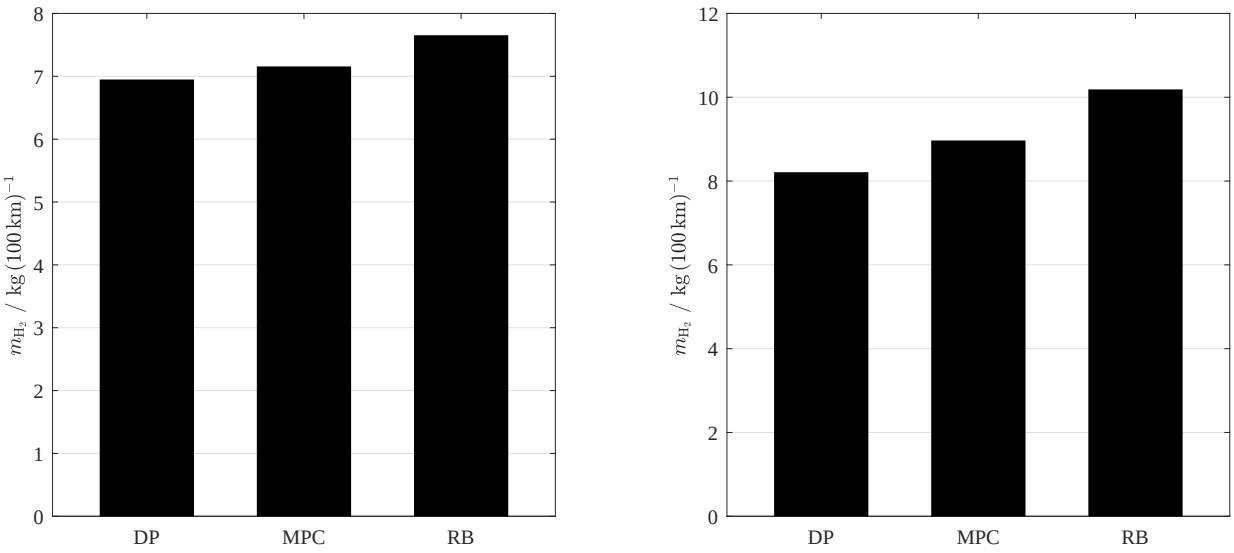


Figure 10. Comparison of the FC system power trajectory and the SoC trajectories between the DP, MPC, and RB control in the MiL environment with the gradient and speed profile of the Aachen-Eifel real driving cycle. The green dashed line indicates the target SoC of 60%.

The magnitude of this correction according to Equation (46) deserves to be quantified. With a terminal SoC of 63.6%, the surplus charge of 3.6 percentage points corresponds to 3.6 kWh of battery energy, which is credited to the MPC as 0.24 kg of hydrogen using the cycle-average fuel cell system efficiency of 45.8%; the uncorrected consumption of 7.90 kg is thus reduced by 3.1% to the reported 7.65 kg. For comparison, the correction amounts to 0.01 kg (0.1%) for the DP with its terminal SoC of 59.9% and to 0.63 kg (6.8%) for the RB strategy, which ends the cycle at 68.1%. The correction does not affect the conclusions drawn from the comparison: it is applied symmetrically to all strategies, the ranking DP–MPC–RB is identical for the uncorrected and the corrected values on both cycles, and in the comparison with the DP it acts in favor of the MPC, which would otherwise consume 14.3%

instead of 10.7% more hydrogen than the DP. Its sensitivity to the assumed conversion efficiency is small; evaluating the credit with the average efficiency of the DP (50.0%) instead of that of the MPC changes the corrected consumption by 0.02 kg or 0.3%.



(**a**) VECTO Long Haul cycle. (**b**) Aachen-Eifel real driving cycle.

Figure 11. Comparison of the corrected hydrogen consumption between the DP, MPC and RB strategies for the (**a**) VECTO Long Haul cycle and the (**b**) Aachen-Eifel real driving cycle.

The terminal deviation itself does not primarily indicate a mismatch between the prediction model and the plant: the same controller with the same models reaches the target SoC within 0.6 percentage points on the VECTO Long Haul cycle (59.4%), and since the states are fed back from the plant at every sampling instant, a model mismatch results in a bias within one horizon rather than in an error that accumulates over the cycle. On the Aachen-Eifel cycle, the deviation originates from the shape of the trajectory in Figure 10. During the uphill section between about 3400 s and 4000 s, the MPC raises the fuel cell power to 244 kW to cover the demand and to restore the SoC within its 400 s horizon. This power is reduced only gradually, because power changes are penalized by the dynamic-stress proxy, while the following downhill section adds recuperated energy, so that the SoC overshoots to 73.1% at $t = 4385$ s. During the remaining approximately 2600 s, the load demand is low and the fuel cell operates predominantly at its lower bound $P_{\mathrm{FCS,min}} = 25$ kW from Equation (39), which is imposed to avoid shutdown and start-stop operation. The surplus can therefore only be reduced at the rate at which the load exceeds $P_{\mathrm{FCS,min}}$, from 13.1 to 3.6 percentage points by the end of the cycle; the RB strategy, which is subject to the same bound, ends the cycle at 68.1% for the same reason. Two properties of the formulation are responsible. The terminal cost in Equation (42) penalizes the SoC deviation at the end of each finite horizon as a soft term and contains no cycle-wide terminal constraint, which would require knowledge of the remaining route that is available to the DP but not to the MPC, and the lower power bound restricts the discharge rate at low load. The offline correction thus serves to compare the consumption of the strategies at an identical charge level; it does not, and is not intended to, improve the closed-loop charge sustaining. Measures for tighter charge sustaining without extending the horizon are an integral SoC feedback term, an adaptive terminal weight, or, where route information is available, a route-based SoC reference trajectory in place of the constant $\mathrm{SoC}_{\mathrm{ref}}$ (see Section 5).

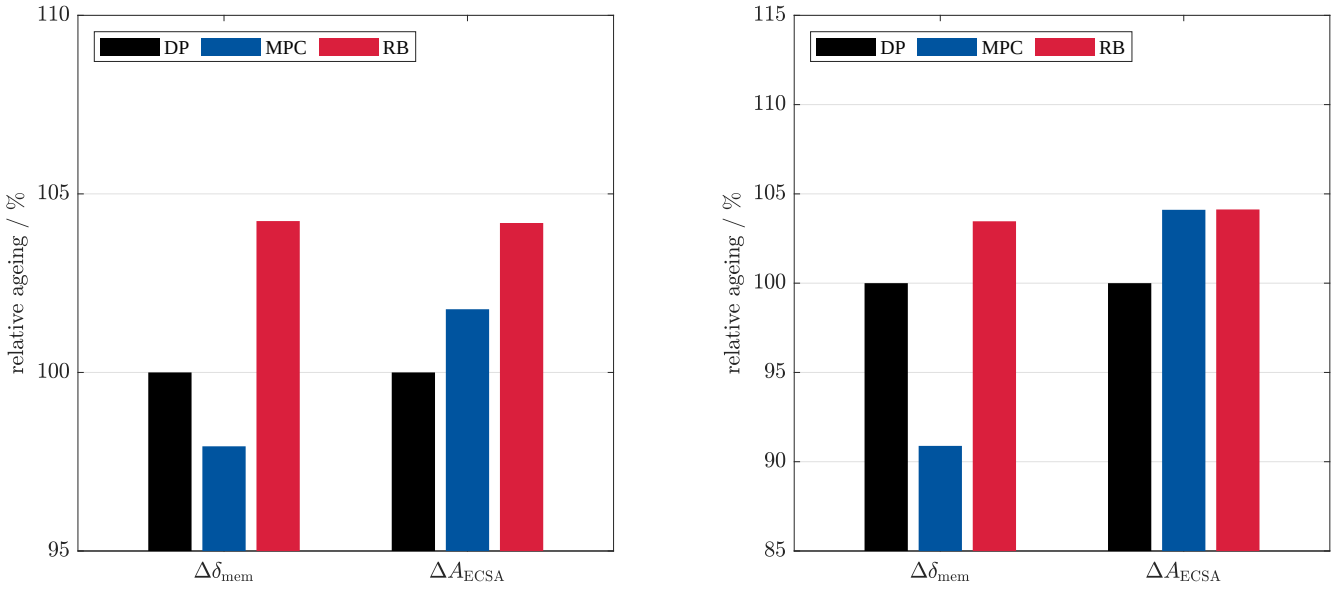
Although the MPC does not reach the global optimum of the DP, it provides the power split in real time. In the next step the MPC is compared to a rule-based strategy.

4.3. MPC vs. Rule-Based Strategy

4.3.1. VECTO Long Haul Cycle

In this section, the MPC is compared to a rule-based (RB) strategy with respect to fuel consumption and end-of-cycle fuel cell stack degradation for the VECTO Long Haul drive cycle. The RB strategy corrects the fuel cell power demand based on the deviation of actual and reference SoC, taking into account the minimum and maximum defined fuel cell power limitations, see Section 3.3. The results of the desired fuel cell power and the SoC trajectory can be seen in Figure 9. Due to the penalization of the SoC deviation in the RB strategy, the power trajectory of the fuel cell is very dynamic, with high power peak demands to minimize the deviation at all times. The power output varies between a minimum of about 25 kW and a maximum of 254.6 kW at $t = 1739$ s. This can also be seen in the trajectory of the SoC with a global minimum SoC of 54.7% at $t = 1692$ s and a maximum SoC of 66.3% due to recuperation at about $t = 2093$ s. Due to the non-predictive characteristic of the RB strategy and the braking process at the end of the cycle, a final SoC above the target SoC of 60% is achieved. The final SoC of the RB strategy is 63.9%, which is 6.4% above the target SoC. After correcting the fuel consumption for the state of charge deviation at the end of the cycle, the total hydrogen consumption of the RB strategy is 7.67 kg, which is 6.9% higher than the MPC's consumption of 7.18 kg.

The end-of-cycle fuel cell degradation is evaluated via the relative membrane thickness change ($\Delta\delta_{\text{mem}}$) and the relative electrochemically active surface area loss (ΔA_{ECSA}), based on the aging model from Thiele et al. [49] and normalized to the DP strategy in Figure 12a. For the VECTO cycle, the dynamic RB strategy exhibits the highest degradation, with a membrane thickness loss 4.2% and an ECSA loss 4.2% above the DP level. The MPC, by contrast, remains close to the globally optimal DP, with a membrane thickness loss 2.1% below and an ECSA loss only 1.8% above the DP level, reflecting its smoother fuel cell power trajectory. The corresponding comparison for the Aachen-Eifel real driving cycle is shown in Figure 12b.



(**a**) VECTO Long Haul cycle. (**b**) Aachen-Eifel real driving cycle.

Figure 12. Comparison of the relative membrane thickness ($\Delta\delta_{\text{mem}}$) and the relative electrochemically active surface area (ΔA_{ECSA}) at the end of the cycle between the DP, MPC, and RB strategies for the (**a**) VECTO Long Haul cycle and the (**b**) Aachen-Eifel real driving cycle.

4.3.2. Aachen-Eifel Real Driving Cycle

In this section, the MPC is compared to a rule-based (RB) strategy with respect to fuel consumption and end-of-cycle fuel cell stack degradation for the Aachen-Eifel real driving cycle. The results of the desired fuel cell power and the SoC trajectory can be seen in Figure 10. Due to the more dynamic elevation and velocity profile, this is also reflected in the power output of the RB strategy, with more fuel cell power peaks to minimize the SoC deviation at all times. This can also be seen in the trajectory of the SoC with a maximum charge deviation down to an SoC of 48.6%. The SoC reaches a maximum value of about 74.4% at $t = 5338\,\mathrm{s}$. The final SoC of the RB strategy is 68.1%, which is 13.5% above the target SoC. After correcting the charge deviation for the RB strategy to the target SoC, the total hydrogen consumption is 8.75 kg, which is 14.3% higher than the MPC's consumption of 7.65 kg. The same trend is observed for the Aachen-Eifel real driving cycle in Figure 12b. The RB strategy again shows the highest degradation, with a membrane thickness loss 3.5% and an ECSA loss 4.1% above the DP level. The MPC attains the lowest membrane thickness loss of all three strategies, 9.1% below the DP level, but reaches an ECSA loss of 4.1% above the DP level. Owing to its smoother power trajectory, the MPC therefore avoids the additional membrane degradation caused by the highly dynamic operation of the RB strategy, whereas in terms of ECSA loss the MPC and the RB strategy are practically on the same level on this cycle.

4.4. Discussion

As shown in Figure 12, the DP achieves the lowest ECSA loss of the three strategies, whereas the MPC exhibits the lowest membrane thickness loss. This can be explained by the fact that the DP predominantly operates at a highly efficient, low-current operating point and therefore at a comparatively high cell voltage, whereas the MPC, due to its limited prediction horizon, more frequently commands higher load points, i.e., lower cell voltages, in order to reach the target SoC at the end of each horizon. Since the formation rate of hydrogen peroxide and the resulting chemical, voltage-dependent membrane degradation (e.g., via the associated fluoride release rate) is known to increase with cell voltage [71], higher operating voltages tend to accelerate membrane degradation. This voltage-dependent chemical degradation pathway is not implemented in the fuel cell model used within the hybrid energy management system in order to limit modeling complexity (see [72] for a broader discussion of prescriptive lifetime management approaches for PEMFC systems). This explains why the DP, despite its higher operating efficiency, does not also achieve the lowest membrane thickness loss. It should be noted that, as a first step, the aging models used in this work have only been checked for plausibility and have not yet been validated against real measurement data.

To assess the transferability of these findings to a different driving profile, all three hybrid strategies were additionally evaluated on the more dynamic Aachen-Eifel real driving cycle (cf. Figures 11b and 12b). The qualitative trends observed for the VECTO Long Haul cycle are confirmed: the DP and the MPC end the cycle close to the target SoC, whereas the non-predictive RB strategy overshoots it by 13.5%, and the ranking of the aging indicators follows the same pattern as for the VECTO cycle. However, the results also reveal that the advantage of the DP over the MPC becomes more pronounced under the more dynamic load profile of the Aachen-Eifel cycle, whereas the MPC achieves a closer approximation of the DP's global optimum on the comparatively steadier VECTO Long Haul cycle.

Regarding applicability to a degraded stack, the methodology remains applicable as long as the MPC prediction model is updated to the actual stack condition. In practice, this can be achieved by (i) initializing the degradation-related state U_{decay} (and/or SoH) to the current value and (ii) updating the polarization-curve-based voltage model (and,

if necessary, the efficiency/BoP maps) to reflect the degraded performance. The OCP structure, constraints, and real-time implementation remain unchanged; only the model parameters and initial conditions need to be adapted. With respect to different powertrain designs, the proposed control strategy is flexible because the OCP formulation is based on generic power and energy balances, component maps, and constraints. A change in component sizing (e.g., stack rated power, battery capacity, DC/DC limits, or auxiliary sizing) primarily affects the steady-state maps (fuel cell efficiency, BoP power) and the admissible operating region (power and SoC constraints), while the MPC structure and real-time implementation remain unchanged. This also makes the approach suitable as a control layer in co-optimization environments: additional objectives (e.g., thermal limits, operating cost, or mission-level constraints) and updated component models can be integrated by extending the stage cost and constraints without changing the underlying solver workflow. Finally, the general MPC/OCP framework is not restricted to heavy-duty road transport and can be adapted to other application domains (e.g., aviation) by replacing the vehicle/mission model, updating constraints and safety requirements, and using domain-specific fuel cell system models.

By smoothing the fuel cell power trajectory, the MPC deliberately shifts the load dynamics to the HV battery. This raises the question of battery degradation under frequent charge–discharge cycling and high C-rates, which is driven by mechanisms such as the growth of the solid electrolyte interphase (SEI), lithium plating and particle cracking [73]. In energy management studies, battery aging is commonly represented by semi-empirical Ah-throughput models that scale the capacity loss with C-rate and temperature [74,75]. Hu et al. [76] extended an MPC for a fuel cell hybrid bus by both fuel cell and battery degradation costs and found the battery degradation cost to be the smallest of the three cost terms, well below the hydrogen and fuel cell degradation costs, although it increased on hilly routes with frequent battery use. The present work focuses on the fuel cell system and therefore does not include a battery aging model; the results quantify the fuel-cell-related potential of the MPC and do not claim optimality with respect to the total cost of ownership. Since the stage cost of the OCP is generic, a battery state-of-health term based on such an Ah-throughput model can be added without changing the solver workflow, and the resulting trade-off between fuel cell and battery aging is a natural extension of this work.

A further simplification concerns the nature of the voltage loss represented by U_{decay}. Measured voltage losses of PEMFC stacks comprise an irreversible part and a reversible part that recovers during shutdown, start-stop, low-load, and open-circuit phases, and recent lifetime prediction approaches separate both contributions [77]. The degradation proxy of this work does not make this distinction. This is justified by the considered horizon: each of the two drive cycles covers a single continuous trip of 1.3–1.9 h in which the fuel cell system is kept running above $P_{\mathrm{FCS,min}}$ (see Equation (39)) and no shutdown, start-stop, or open-circuit events occur, i.e., the operating conditions to which the recovery of reversible losses is coupled are absent by design. Within this horizon, the proxy therefore penalizes dynamic operation as a driver of the irreversible mechanical and chemical degradation pathways that are evaluated in Figure 12, and no reversible share is penalized in excess.

Finally, the stack temperature is not a state of the controller model, although the durability of PEMFC stacks is known to be temperature-sensitive and adaptive, temperature-dependent SoH characteristics have been proposed to exploit this sensitivity [78]. This reflects the control hierarchy of the vehicle rather than a neglect of thermal effects. The MPC presented here is a supervisory energy management at the vehicle level: it decides on the power split between the fuel cell system and the battery. The thermal management of the stack is the task of the subordinate control loops of the FCCU at the fuel cell system level, which regulate the stack temperature to its set point via the coolant circuit (Section 2). At

the vehicle level, the stack temperature is therefore a controlled quantity and not a degree of freedom of the power split, and the isothermal controller model is consistent with this separation. The thermal behavior is nevertheless contained in the plant model, whose segmented thermal model resolves the actual stack temperature and its effect on the local operating conditions, so that the evaluation of the strategies is not isothermal.

5. Conclusions

In this work, a degradation-aware nonlinear MPC was developed that computes the fuel cell power trajectory of a heavy-duty fuel cell truck by solving an OCP with the open-source software package `acados` in `MATLAB Simulink`, with the hydrogen consumption, a dynamic-stress proxy of the fuel cell power, the electrochemical efficiency, and the terminal SoC deviation as cost terms. Based on a parameter analysis of the prediction horizon, a horizon of 400 s was identified as the compromise between execution time, hydrogen consumption, deviation from the target SoC and cell voltage loss. The MPC was implemented in a model-in-the-loop environment and evaluated on the VECTO Long Haul cycle and the Aachen-Eifel real driving cycle against a globally optimal DP as the upper bound of the achievable performance and against a rule-based strategy that does not account for degradation.

On the VECTO Long Haul cycle, the DP consumes 2.9% less hydrogen than the MPC; on the more dynamic Aachen-Eifel real driving cycle, the MPC consumes 10.7% more hydrogen than the DP. The advantage of the global optimum thus becomes more pronounced under dynamic load profiles, whereas the MPC closely approaches the DP on the steadier long-haul profile. Compared with the MPC, the RB strategy consumes 6.9% (VECTO Long Haul) and 14.3% (Aachen-Eifel) more hydrogen. The MPC ends the cycles at −1.06% (VECTO Long Haul) and +6.1% (Aachen-Eifel) of the target SoC, whereas the non-predictive RB strategy overshoots the target by 6.4% and 13.5%, respectively. By penalizing the power gradient in the cost function, the MPC avoids large power fluctuations of the fuel cell system and thereby reduces the end-of-cycle degradation relative to the RB strategy: on the VECTO Long Haul cycle, the membrane thickness loss and the ECSA loss of the MPC are 6.1% and 2.3% lower than those of the RB strategy; on the Aachen-Eifel real driving cycle, the membrane thickness loss is 12.2% lower, whereas the ECSA loss of both strategies is practically identical. The DP attains the lowest ECSA loss of the three strategies, whereas the MPC attains the lowest membrane thickness loss, because the DP operates predominantly at high cell voltage, where the voltage-dependent chemical membrane degradation is accelerated. The real-time capability of the approach was verified on a dSPACE MicroAutoBox III: with the selected horizon of 400 s, the MPC task requires 158.2 ms on average within its 300 ms task; the execution time increases only in the terminal phase of the cycle with tightened power bounds, and the closed-loop trajectories coincide with those of the MiL simulation.

The degradation term of the MPC is based on a dynamic-stress proxy of the fuel cell power trajectory, which drives an empirically parameterized cell voltage decay within the controller, whereas the ageing assessment of the strategies relies on the membrane thickness and ECSA losses of the physics-based aging model of the plant. The degradation results are therefore to be read as a relative comparison of the strategies on an identical plant and aging model, whose parameters are taken from the literature and have not yet been validated against measurements of the stack considered; the empirical decay coefficient of the proxy is used without recalibration, which affects the controller-internal voltage decay but neither the optimization result nor the reported degradation indicators.

For real driving, where the speed profile cannot be followed exactly, telemetry data and a predictive driving profile model, e.g., a Markov chain model, would have to provide the profile information to the MPC. For multi-day missions with parking and start-stop phases, the degradation proxy should further be extended to distinguish reversible from

irreversible voltage losses, so that the recovery of reversible losses is not penalized by the controller. Beyond the vehicle-level power split considered here, a coordination with the control at the fuel cell system level, e.g., by a temperature-dependent weighting of the degradation term or by passing the thermal state of the stack to the MPC, is a further step towards a durability-oriented control of the complete fuel cell powertrain. For tighter charge sustaining on routes with pronounced elevation changes, where the terminal SoC of the MPC deviated by 3.6 percentage points from its target on the Aachen-Eifel cycle, an integral SoC feedback term, an adaptive terminal weight, or a route-based SoC reference trajectory can be added to the OCP without changing the solver workflow.

Author Contributions: Conceptualization, S.M., A.W. and S.P.; methodology, S.M.; software, S.M. and A.W.; validation, S.M., A.W. and S.P.; formal analysis, S.M.; investigation, S.M.; resources, V.S. and J.S.; data curation, S.M.; writing—original draft preparation, S.M.; writing—review and editing, S.M., A.W., V.S., J.S., A.E. and S.P.; visualization, S.M.; supervision, S.P. and A.E.; project administration, S.P.; funding acquisition, S.P. All authors have read and agreed to the published version of the manuscript.

Funding: The presented work has been done as part of the research project "ReforceHIL" (03EN5004A-C) that is supported within the 7th Energy Research Program: Innovations for Energy Transition by the Federal Ministry for Economic Affairs and Climate Action. The APC was funded by RWTH Aachen University.

Institutional Review Board Statement: Not applicable.

Informed Consent Statement: Not applicable.

Data Availability Statement: Data are contained within the article.

Acknowledgments: The authors gratefully acknowledge the support of the ReforceHIL project partners.

Conflicts of Interest: Authors Vivek Srivastava and Joschka Schaub are employed by the FEV Europe GmbH. The work was conducted as joint research. The authors declare that the research was conducted in the absence of any commercial or financial relationships that could be construed as a potential conflict of interest.

Nomenclature

The following symbols are used in this manuscript. Subscripts min, max, ref, act, and 0 denote minimum, maximum, reference, actual, and initial values, respectively; the subscripts BoL and EoL refer to the beginning and the end of life of the fuel cell stack.

a_v	vehicle acceleration	$m\,s^{-2}$
$a_0 \dots a_6$	coefficients of the electrical machine loss map	–
A	weighting of the terminal cost (Equation (42))	–
A_{proj}	projected frontal area of the vehicle	m^2
c_w	aerodynamic drag coefficient	–
C_{bat}, C_{cell}	capacity of the battery pack and of a single cell	Ah
C_{batt}	energy content of the battery (H_2 correction)	kWh
f_r	rolling resistance coefficient	–
F	Faraday constant	$C\,mol^{-1}$
F_{air}, F_r, F_g, F_a, F_t	aerodynamic, rolling, grade, acceleration and total driving resistance	N
g	gravitational acceleration	$m\,s^{-2}$
G	weighting matrix of the slack variables	–
H	prediction horizon	s
H_{u,H_2}	lower heating value of hydrogen	$J\,kg^{-1}$
I_{St}	stack current	A
$I_{bat,act}$	battery pack current (positive when discharging)	A
J	cost function of the OCP	–
k	discrete time index within the horizon	–

m_v	vehicle mass	kg
m_{H_2}, $\dot{m}_{H_2}$	consumed hydrogen mass and hydrogen mass flow	kg, kg s^{-1}
M_{H_2}	molar mass of hydrogen	kg mol^{-1}
n_{em}	rotational speed of the electrical machine	min^{-1}
$n_{bat,ser}$, $n_{bat,par}$	number of battery cells in series and parallel	–
N_p	number of shooting nodes in the prediction horizon	–
P_{FC}	gross power of the fuel cell stack	W
P_{FCS}	net power of the fuel cell system	W
ΔP_{FCS}	rate of change of the fuel cell system power (control input u)	W s^{-1}
P_{BoP}	power of the balance-of-plant auxiliaries	W
P_{bat}, $P_{bat,act}$	battery power	W
P_{em}, $P_{em_{loss}}$	power and power loss of the electrical machine	W
P_t, P_{prop}	traction power at the wheel and propulsion power	W
P_{el}	net electrical output power of the fuel cell system	W
Q, Y, W	weighting and scaling of the stage cost and of the terminal cost	–
R_{int}, $R_{int,dis}$, $R_{int,chr}$	internal resistance of the pack, of a cell when discharging and when charging	Ω
SoC	state of charge of the battery	–
SoH	state of health of the fuel cell stack	–
t, t_{CPU}	time and execution time of the OCP solver	s
T_{bat}	battery temperature	°C
T_{em}	torque of the electrical machine	N m
u	control input of the OCP	W s^{-1}
u_{decay}, U_{decay}	cell voltage decay rate and accumulated cell voltage decay	V s^{-1}, V
u_{OCV}, U_{OCV}	open circuit voltage of a battery cell and of the pack	V
U_A, $U_{A,act}$, $U_{A,BoL}$, $U_{A,EoL}$	cell voltage (working voltage) and its actual, beginning-of-life and end-of-life values	V
U_N, U_{rev}	Nernst voltage and reversible cell voltage	V
ΔU, ΔU_{Act}, ΔU_{Ohm}, ΔU_{Conc}	total, activation, ohmic and concentration voltage losses	V
U_{St}	stack voltage	V
$U_{bat,act}$	terminal voltage of the battery pack	V
v, v_{act}	vehicle velocity	m s^{-1}
x	state vector of the OCP	–
z	number of electrons transferred per reaction	–
α	road slope angle	rad
$\beta(k)$	vector of stage cost terms	–
δ_{mem}, $\Delta\delta_{mem}$	membrane thickness and its relative change	m, %
ΔA_{ECSA}	relative loss of electrochemically active surface area	%
ϵ_1, ϵ_2	slack variables of the cell voltage constraints	V
η_{Fc}, $\eta_{ec,Fc}$	system efficiency and electrochemical efficiency of the fuel cell	–
η_{inv}, η_{gb}, η_{dif}, $\eta_{dcdc,Fc}$, η_{bat}	efficiencies of inverter, gearbox, differential, fuel cell DC/DC converter, and battery	–
ρ_{air}	air density	kg m^{-3}
σ, σ_{MPC}	dynamic-stress proxy of the fuel cell power	–

Abbreviations

The following abbreviations are used in this manuscript:

ACL	Anode Catalyst Layer
A-ECMS	Adaptive Equivalent Consumption Minimization Strategy
BoL	Beginning of Life
BoP	Balance of Plant
CCL	Cathode Catalyst Layer
CU	Control Unit
DC	Direct Current
DP	Dynamic Programming
ECMS	Equivalent Consumption Minimization Strategy

ECSA	Electrochemically Active Surface Area
EF	Equivalence Factor
EM	Electrical Machine
EMS	Energy Management Strategy
EoL	End of Life
ERK	Explicit Runge–Kutta
ESS	Energy Storage System
EV	Electric Vehicle
FC	Fuel Cell
FCCU	Fuel Cell Control Unit
FCEV	Fuel Cell Electric Vehicle
FL	Fuzzy Logic
GDL	Gas Diffusion Layer
HCU	Hybrid Control Unit
HDV	Heavy-Duty Vehicle
HPIPM	High-Performance Interior-Point Method
HV	High-Voltage
HWFET	Highway Fuel Economy Test
KKT	Karush-Kuhn-Tucker
LB	Learning-Based
MEA	Membrane Electrode Assembly
MiL	Model-in-the-Loop
MPC	Model Predictive Control
MPL	Micro-Porous Layer
NOP	Nonlinear Optimization Problem
OB	Optimization-Based
OCP	Optimal Control Problem
OCV	Open Circuit Voltage
PEMFC	Proton Exchange Membrane Fuel Cell
PI	Proportional-Integral
PMP	Pontryagin's Minimum Principle
QP	Quadratic Programming
RB	Rule-Based
RCP	Rapid Control Prototyping
RHC	Receding Horizon Control
RL	Reinforcement Learning
SC	Supercapacitor
SDP	Stochastic Dynamic Programming
SEI	Solid Electrolyte Interphase
SoC	State of Charge
SoH	State of Health
SQP	Sequential Quadratic Programming
VECTO	Vehicle Energy Consumption Calculation Tool

References

1. United Nations Framework Convention on Climate Change. Adoption of the Paris Agreement, Decision 1/CP.21. In *Report of the Conference of the Parties on Its Twenty-First Session, Held in Paris from 30 November to 13 December 2015, Addendum; FCCC/CP/2015/10/Add.1*; UNFCCC: Bonn, Germany, 2016. Available online: https://unfccc.int/resource/docs/2015/cop21/eng/10a01.pdf (accessed on 20 September 2026).
2. European Parliament Backs CO_2 Emissions Cuts for Trucks. Press Release 20181106IPR18331, 14 November 2018. Available online: https://www.europarl.europa.eu/news/en/press-room/20181106IPR18331/european-parliament-backs-co2-emissions-cuts-for-trucks (accessed on 20 September 2026).
3. Colnago, S.; Mauri, M.; Piegari, L. Energy Management Strategy for a Fuel cell/Lead acid battery/Ultracapacitor hybrid electric vehicle. In Proceedings of the 2020 IEEE Vehicle Power and Propulsion Conference (IEEE VPPC 2020), Virtual, 18 November–16 December 2020. [CrossRef]

4. Silvas, E.; Hofman, T.; Murgovski, N.; Etman, P.; Steinbuch, M. Review of Optimization Strategies for System-Level Design in Hybrid Electric Vehicles. *Renew. Sustain. Energy Rev.* **2020**, *119*, 109596. [CrossRef]
5. Abad, A.V.; Dodds, P.E. Green hydrogen characterisation initiatives: Definitions, standards, guarantees of origin, and challenges. *Energy Policy* **2020**, *138*, 111300. [CrossRef]
6. Tran, D.D.; Vafaeipour, M.; El Baghdadi, M.; Barrero, R.; van Mierlo, J.; Hegazy, O. Thorough state-of-the-art analysis of electric and hybrid vehicle powertrains: Topologies and integrated energy management strategies. *Renew. Sustain. Energy Rev.* **2020**, *119*, 109596. [CrossRef]
7. Yu, P.; Li, M.; Wang, Y.; Chen, Z. Fuel Cell Hybrid Electric Vehicles: A Review of Topologies and Energy Management Strategies. *World Electr. Veh. J.* **2022**, *13*, 172. [CrossRef]
8. Emran, A.; Garg, S.; Mertes, S.; Gautam, A.; Schmidt, M.; Wick, M.; Walters, M.; Wagh, S.; Sharma, V. Fuel Cell Electric Metro Train Concept—Zero Emission Rail Transport Solution for Indian Cities. *Int. J. Adv. Curr. Pract. Mobil.* **2024**, *6*, 2954–2964. [CrossRef]
9. Jia, H.; Tang, J.; Yu, Y.; Sun, Y.; Yin, B.; Zhang, C. Energy Management Strategy of Fuel Cell/Battery Hybrid Vehicle Based on Series Fuzzy Control. *Int. J. Automot. Technol.* **2021**, *22*, 1545–1556. [CrossRef]
10. Biswas, A.; Emadi, A. Energy Management Systems for Electrified Powertrains: State-of-the-Art Review and Future Trends. *IEEE Trans. Veh. Technol.* **2019**, *68*, 6453–6467. [CrossRef]
11. Azib, T.; Bethoux, O.; Remy, G.; Marchand, C.; Berthelot, E. An Innovative Control Strategy of a Single Converter for Hybrid Fuel Cell/Supercapacitor Power Source. *IEEE Trans. Ind. Electron.* **2010**, *57*, 4024–4031. [CrossRef]
12. Ragab, A.; Marei, M.I.; Mokhtar, M. Adaptive energy management strategy for fuel cell hybrid electric vehicles using a hybrid controller. *Electr. Power Syst. Res.* **2026**, *259*, 113197. [CrossRef]
13. Fu, Z.; Li, Z.; Si, P.; Tao, F. A hierarchical energy management strategy for fuel cell/battery/supercapacitor hybrid electric vehicles. *Int. J. Hydrogen Energy* **2019**, *44*, 22146–22159. [CrossRef]
14. Geng, B.; Mills, J.K.; Sun, D. Two-Stage Energy Management Control of Fuel Cell Plug-In Hybrid Electric Vehicles Considering Fuel Cell Longevity. *IEEE Trans. Veh. Technol.* **2012**, *61*, 498–508. [CrossRef]
15. Murphey, Y.L.; Chen, Z.; Kiliaris, L.; Masrur, M.A. Intelligent power management in a vehicular system with multiple power sources. *J. Power Sources* **2011**, *196*, 835–846. [CrossRef]
16. Li, W.; Ye, J.; Cui, Y.; Kim, N.; Cha, S.W.; Zheng, C. A Speedy Reinforcement Learning-Based Energy Management Strategy for Fuel Cell Hybrid Vehicles Considering Fuel Cell System Lifetime. *Int. J. Precis. Eng. Manuf.-Green Technol.* **2022**, *9*, 859–872. [CrossRef]
17. Mei, J.; Li, Z.; Song, K.; Meng, X.; Wu, H.; Tang, X.; Hasanien, H.M.; Li, Y.; Sun, C. SOH-Disparity-Aware Energy Management for Multi-Stack Fuel Cells Using Enhanced Soft Actor-Critic Reinforcement Learning. *IEEE Trans. Transp. Electrif.* **2026**, *early access*. [CrossRef]
18. Zhu, Y.; Li, X.; Liu, Q.; Li, S.; Xu, Y. Review article: A comprehensive review of energy management strategies for hybrid electric vehicles. *Mech. Sci.* **2022**, *13*, 147–188. [CrossRef]
19. Yang, S.; Ghate, A.; Zhu, Q.; Prucka, R. An interpretable reinforcement learning approach for emission and fuel optimization in heavy-duty hybrid electric vehicles. *Energy Convers. Manag.* **2025**, *347*, 120459. [CrossRef]
20. Salay, R.; Queiroz, R.; Czarnecki, K. An Analysis of ISO 26262: Using Machine Learning Safely in Automotive Software. *arXiv* **2017**, arXiv:1709.02435. [CrossRef]
21. Liu, X.; Srivastava, V.; Pan, W.; Schaub, J.; Sun, J.; Tian, X.; Deng, Y.; Xiong, J.; Wu, X.; Muthyala, P.; et al. Real-time Multi-Layer Predictive Energy Management for a Plug-in Hybrid Vehicle based on Horizon and Navigation Data. In Proceedings of the WCX SAE World Congress Experience, Detroit, MI, USA, 16–18 April 2024. [CrossRef]
22. Chen, Z.; Guo, N.; Zhang, Q.; Shen, J.; Xiao, R. An Optimized Rule Based Energy Management Strategy for a Fuel Cell/Battery Vehicle. In Proceedings of the 2017 IEEE Vehicle Power and Propulsion Conference (VPPC), Belfort, France, 11–17 December 2017; pp. 1–6. [CrossRef]
23. Zhou, Y.; Ravey, A.; Péra, M.C. Real-time cost-minimization power-allocating strategy via model predictive control for fuel cell hybrid electric vehicles. *Energy Convers. Manag.* **2021**, *229*, 113721. [CrossRef]
24. Ferrara, A.; Hametner, C.; Jakubek, S. Health-conscious predictive energy management strategy for fuel cell electric trucks. *Energy Rep.* **2024**, *12*, 5961–5973. [CrossRef]
25. Ferrara, A.; Jakubek, S.; Hametner, C. Cost-optimal design and energy management of fuel cell electric trucks. *Int. J. Hydrogen Energy* **2023**, *48*, 16420–16434. [CrossRef]
26. Hemi, H.; Ghouili, J.; Cheriti, A. Combination of Markov chain and optimal control solved by Pontryagin's Minimum Principle for a fuel cell/supercapacitor vehicle. *Energy Convers. Manag.* **2015**, *91*, 387–393. [CrossRef]
27. Bernard, J.; Delprat, S.; Buechi, F.; Guerra, T.M. Global Optimisation in the power management of a Fuel Cell Hybrid Vehicle (FCHV). In Proceedings of the 2006 IEEE Vehicle Power and Propulsion Conference, Windsor, UK, 6–8 September 2006; pp. 1–6. [CrossRef]

28. Song, K.; Wang, X.; Li, F.; Sorrentino, M.; Zheng, B. Pontryagin's minimum principle-based real-time energy management strategy for fuel cell hybrid electric vehicle considering both fuel economy and power source durability. *Energy* **2020**, *205*, 118064. [CrossRef]
29. Huangfu, Y.; Li, P.; Pang, S.; Tian, C.; Quan, S.; Zhang, Y.; Wei, J. An Improved Energy Management Strategy for Fuel Cell Hybrid Vehicles Based on Pontryagin's Minimum Principle. *IEEE Trans. Ind. Appl.* **2022**, *58*, 4086–4097. [CrossRef]
30. Aubeck, F. Modulary Structured Optimization of the Energy Management in Hybrid Vehicles. Ph.D. Thesis, Rheinisch-Westfälischen Technischen Hochschule Aachen, Aachen, Germany, 2022.
31. Zhang, Y.; Chen, M.; Cai, S.; Hou, S.; Yin, H.; Gao, J. An online energy management strategy for fuel cell hybrid vehicles. In Proceedings of the 2021 40th Chinese Control Conference (CCC), Shanghai, China, 26–28 July 2021; pp. 6034–6039. [CrossRef]
32. Muthyala, P.; Mayank, M.; Ünver, B.; Han, S.E.; Uzunoğlu, B.; Kaydeci, A.B.; Toğuş, F.; Schaub, J.; Virnich, L.; Pischinger, S. Comparative study of real-time A-ECMS and rule-based energy management strategies in long haul heavy-duty PHEVs. *Energy Convers. Manag. X* **2024**, *23*, 100679. [CrossRef]
33. Arce, A.; del Real, A.J.; Bordons, C. MPC for battery/fuel cell hybrid vehicles including fuel cell dynamics and battery performance improvement. *J. Process Control* **2009**, *19*, 1289–1304. [CrossRef]
34. Li, T.; Liu, H.; Ding, D. Predictive energy management of fuel cell supercapacitor hybrid construction equipment. *Energy* **2018**, *149*, 718–729. [CrossRef]
35. Desantes, J.M.; Novella, R.; Lopez-Juarez, M.; Nidaguila, I. Experimental assessment of a heavy-duty fuel cell system in relevant operating conditions. *Appl. Energy* **2024**, *376*, 124293. [CrossRef]
36. Aliberti, P.; Minneci, M.; Sorrentino, M.; Cuomo, F.; Musto, C. Efficiency-Based Modeling of Aeronautical Proton Exchange Membrane Fuel Cell Systems for Integrated Simulation Framework Applications. *Energies* **2025**, *18*, 999. [CrossRef]
37. Aliberti, P.; Simone, C.; Addesso, P.; Piano, G.D.; Dons'i, F.; Galdi, A.; Maritato, L.; Pantani, R.; Pianese, C.; Polverino, P.; et al. Fuel cells in aviation: Challenges to power the future of flight. *Energy Convers. Manag. X* **2026**, *29*, 101426. [CrossRef]
38. Xu, N.; Kong, Y.; Chu, L.; Ju, H.; Yang, Z.; Xu, Z.; Xu, Z. Towards a Smarter Energy Management System for Hybrid Vehicles: A Comprehensive Review of Control Strategies. *Appl. Sci.* **2019**, *9*, 2026. [CrossRef]
39. Frey, J.; Baumgärtner, K.; Frison, G.; Diehl, M. Multi-Phase Optimal Control Problems for Efficient Nonlinear Model Predictive Control with acados. *arXiv* **2024**, arXiv:2408.07382.
40. Verschueren, R.; Frison, G.; Kouzoupis, D.; Frey, J.; van Duijkeren, N.; Zanelli, A.; Novoselnik, B.; Albin, T.; Quirynen, R.; Diehl, M. acados—A modular open-source framework for fast embedded optimal control. *Math. Program. Comput.* **2021**, *14*, 147–183. [CrossRef]
41. Srivastava, V.; Wendler, A.; Schaub, J.; Walters, M.; Thodupunoori, S.; Mulukutla, K. Modular Fuel Cell Control Software for Commercial Vehicle Applications. In Proceedings of the Symposium on International Automotive Technology, Moshi, India, 23–25 January 2024. [CrossRef]
42. Emran, A.; Mertes, S.; Garg, S.; Wick, M.; Walters, M.; Sharma, V. Fuel Cell Electric Vehicles—An Optimal Solution for Future Electrification of Heavy Commercial Vehicles in India. In Proceedings of the 2021 IEEE Transportation Electrification Conference (ITEC-India), Manesar, India, 16–18 December 2021; pp. 1–8. [CrossRef]
43. Tinz, S.; Wick, M.; Gößling, S.; Bahr, M. Modular Fuel Cell System Simulation Environment with Focus on Membrane Water Management. *MTZ Worldw.* **2022**, *83*, 52–57. [CrossRef]
44. Sallach, D.; Weber, N.; Cäsar, J.; Hinrichs, N.; Ennen, A.; Mertes, S.; Pischinger, S.; Kampker, A.; Vallery, H.; Jeschke, P. *Report (Final Report of the HyInnoPEM Project)*; HyInnoPEM Technische Informationsbibliothek (TIB): Hannover, Germany, 2025. [CrossRef] [PubMed]
45. Liu, Y.; Dirkes, S.; Kohrn, M.; Wick, M.; Pischinger, S. A high-fidelity real-time capable dynamic discretized model of proton exchange membrane fuel cells for the development of control strategies. *J. Power Sources* **2022**, *537*, 231394. [CrossRef]
46. Dickinson, E.J.F.; Smith, G. Modelling the Proton-Conductive Membrane in Practical Polymer Electrolyte Membrane Fuel Cell (PEMFC) Simulation: A Review. *Membranes* **2020**, *10*, 310. [CrossRef] [PubMed]
47. Satterfield, M.B.; Benziger, J.B. Non-Fickian water vapor sorption dynamics by Nafion membranes. *J. Phys. Chem. B* **2008**, *112*, 3693–3704. [CrossRef] [PubMed]
48. Colpan, C.O.; Nalbant, Y.; Ercelik, M. 4.28 Fundamentals of Fuel Cell Technologies. In *Comprehensive Energy Systems*; Dincer, I., Ed.; Elsevier: Oxford, UK, 2018; pp. 1107–1130. [CrossRef]
49. Thiele, P.; Gouveia, L.; Ulrich, O.; Yang, Y.; Liu, Y.; Wick, M.; Pischinger, S. Realistic accelerated stress tests for PEM fuel cells: Operation condition dependent load profile optimization. *J. Power Sources* **2024**, *617*, 234959. [CrossRef]
50. Lenz, M.; Mertes, S.; Beecks, P.-J.; Viertel, P.; Pischinger, S. Generating characteristic maps of battery cell parameters from sparse input data. *J. Power Sources* **2021**, *503*, 230054. [CrossRef]
51. Lenz, M.; Hoehl, T.; Mertes, S.; Pischinger, S. Applying a numerical optimization to determine the entropic heat coefficient of a battery. *Appl. Therm. Eng.* **2022**, *211*, 118467. [CrossRef]

52. Dirk Abel, A.B. *Rapid Control Prototyping: Methoden und Anwendungen*; Springer Berlin Heidelberg: Berlin/Heidelberg, Germany, 2006. [CrossRef]
53. The MathWorks, Inc. MATLAB/Simulink, Release R2021b; The MathWorks, Inc.: Natick, MA, USA, 2021. Available online: https://www.mathworks.com/products/simulink.html (accessed on 20 September 2026).
54. Coralli, A.; Sarruf, B.J.; de Miranda, P.E.V.; Osmieri, L.; Specchia, S.; Minh, N.Q. Fuel Cells. In *Science and Engineering of Hydrogen-Based Energy Technologies*; Elsevier: Amsterdam, The Netherlands, 2019. [CrossRef]
55. Lin, X.; Xu, X.; Lin, H. Predictive-ECMS based degradation protective control strategy for a fuel cell hybrid electric vehicle considering uphill condition. *eTransportation* **2022**, *12*, 100168. [CrossRef]
56. Stevens, M. Hybrid Fuel Cell Vehicle Powertrain Development Considering Power Source Degradation. Ph.D. Thesis, University of Waterloo, Waterloo, ON, Canada, 2009.
57. Jouin, M.; Bressel, M.; Morando, S.; Gouriveau, R.; Hissel, D.; Péra, M.C.; Zerhouni, N.; Jemei, S.; Hilairet, M.; Bouamama, B.O. Estimating the end-of-life of PEM fuel cells: Guidelines and metrics. *Appl. Energy* **2016**, *177*, 87–97. [CrossRef]
58. Lin, C.-C.; Peng, H.; Grizzle, J.W.; Kang, J.-M. Power management strategy for a parallel hybrid electric truck. *IEEE Trans. Control Syst. Technol.* **2003**, *11*, 839–849. [CrossRef]
59. Hsieh, Y.M.; Liu, Y.C. Model predictive control strategy for plug-in hybrid electric vehicles. In Proceedings of the 2016 14th International Conference on Control, Automation, Robotics and Vision (ICARCV), Phuket, Thailand, 13–15 November 2016; pp. 1–6. [CrossRef]
60. acados. acados: Fast and Embedded Solvers for Nonlinear Optimal Control, Version 0.4.5. 2025. Available online: https://github.com/acados/acados/releases/tag/v0.4.5 (accessed on 20 September 2026).
61. Papageōrgiu, M.; Leibold, M.; Buss, M. *Optimierung: Statische, Dynamische, Stochastische Verfahren für die Anwendung*, 4th ed.; Springer Vieweg: Berlin/Heidelberg, Germany, 2015.
62. Vehicle Energy Consumption calculation TOol—VECTO. 2017. Available online: https://climate.ec.europa.eu/eu-action/transport/road-transport-reducing-co2-emissions-vehicles/vehicle-energy-consumption-calculation-tool-vecto_en (accessed on 20 September 2026).
63. Jahnke, T.; Futter, G.A.; Baricci, A.; Rabissi, C.; Casalegno, A. Physical Modeling of Catalyst Degradation in Low Temperature Fuel Cells: Platinum Oxidation, Dissolution, Particle Growth and Platinum Band Formation. *J. Electrochem. Soc.* **2020**, *167*, 013523. [CrossRef]
64. You, H.; Fu, J.; Li, X. Research on ECSA Degradation Model for PEM Fuel Cell under Vehicle Conditions. In Proceedings of the 2020 4th CAA International Conference on Vehicular Control and Intelligence (CVCI), Hangzhou, China, 18–20 December 2020. [CrossRef]
65. Ma, Y.; Zhang, J.; Yang, K.; Lin, Q.; Sun, B.; Hu, Z.; Zhai, S. Data-driven electrochemically active surface area loss modeling and its application in fuel cell stack degradation prediction. *J. Power Sources* **2025**, *659*, 238354. [CrossRef]
66. Pei, P.; Chang, Q.; Tang, T. A quick evaluating method for automotive fuel cell lifetime. *Int. J. Hydrogen Energy* **2008**, *33*, 3829–3836. [CrossRef]
67. Pei, P.; Chen, H. Main factors affecting the lifetime of Proton Exchange Membrane fuel cells in vehicle applications: A review. *Appl. Energy* **2014**, *125*, 60–75. [CrossRef]
68. dSPACE. MicroAutoBox III. dSPACE GmbH: Paderborn, Germany. Available online: https://www.dspace.com/en/pub/home/products/hw/micautob/microautobox3.cfm (accessed on 21 September 2026).
69. dSPACE. SCALEXIO. dSPACE GmbH: Paderborn, Germany. Available online: https://www.dspace.com/en/pub/home/products/hw/simulator_hardware/scalexio.cfm (accessed on 21 September 2026).
70. Aubeck, F.; Lenz, M.; Mertes, S.; Zylka, K.; Pischinger, S. Generic stochastic particle filter algorithm for predictive energy optimization of a Plug-in Hybrid Electric Vehicle extended by a battery temperature control and implemented on a Hardware-in-the-Loop system. *Control Eng. Pract.* **2022**, *120*. [CrossRef]
71. Dirkes, S.; Leidig, J.; Fisch, P.; Pischinger, S. Prescriptive Lifetime Management for PEM Fuel Cell Systems in Transportation Applications, Part II: On-board Operando Feature Extraction, Condition Assessment and Lifetime Prediction. *Energy Convers. Manag.* **2023**, *283*, 116943. [CrossRef]
72. Dirkes, S.; Leidig, J.; Fisch, P.; Pischinger, S. Prescriptive Lifetime Management for PEM Fuel Cell Systems in Transportation Applications, Part I: State of the Art and Conceptual Design. *Energy Convers. Manag.* **2023**, *277*, 116598. [CrossRef]
73. Edge, J.S.; O'Kane, S.; Prosser, R.; Kirkaldy, N.D.; Patel, A.N.; Hales, A.; Ghosh, A.; Ai, W.; Chen, J.; Yang, J.; et al. Lithium ion battery degradation: What you need to know. *Phys. Chem. Chem. Phys.* **2021**, *23*, 8200–8221. [CrossRef] [PubMed]
74. Wang, J.; Liu, P.; Hicks-Garner, J.; Sherman, E.; Soukiazian, S.; Verbrugge, M.; Tataria, H.; Musser, J.; Finamore, P. Cycle-life model for graphite-LiFePO4 cells. *J. Power Sources* **2011**, *196*, 3942–3948. [CrossRef]
75. Ebbesen, S.; Elbert, P.; Guzzella, L. Battery State-of-Health Perceptive Energy Management for Hybrid Electric Vehicles. *IEEE Trans. Veh. Technol.* **2012**, *61*, 2893–2900. [CrossRef]

76. Hu, X.; Zou, C.; Tang, X.; Liu, T.; Hu, L. Cost-Optimal Energy Management of Hybrid Electric Vehicles Using Fuel Cell/Battery Health-Aware Predictive Control. *IEEE Trans. Power Electron.* **2020**, *35*, 382–392. [CrossRef]
77. Meng, X.; Sun, C.; Mei, J.; Tang, X.; Hasanien, H.M.; Jiang, J.; Fan, F.; Song, K. Fuel cell life prediction considering the recovery phenomenon of reversible voltage loss. *J. Power Sources* **2025**, *625*, 235634. [CrossRef]
78. Tang, X.; Yang, M.; Shi, L.; Hou, Z.; Xu, S.; Sun, C. Adaptive state-of-health temperature sensitivity characteristics for durability improvement of PEM fuel cells. *Chem. Eng. J.* **2024**, *491*, 151951. [CrossRef]

Disclaimer/Publisher's Note: The statements, opinions and data contained in all publications are solely those of the individual author(s) and contributor(s) and not of MDPI and/or the editor(s). MDPI and/or the editor(s) disclaim responsibility for any injury to people or property resulting from any ideas, methods, instructions or products referred to in the content.